# A GNSS velocity field for geophysical applications in Fennoscandia

Halfdan Pascal Kierulf [a,b,*], Holger Steffen [c], Valentina R. Barletta [d], Martin Lidberg [c], Jan Johansson [e], Oddgeir Kristiansen [f], Lev Tarasov [g]

[a] *Geodetic Institute, Norwegian Mapping Authority, Hønefoss, Norway*
[b] *Department of Geosciences, University of Oslo, Oslo, Norway*
[c] *Lantmäteriet, Gävle, Sweden*
[d] *DTU Space, Lyngby, Denmark*
[e] *Chalmers Tekniska Högskola, Gothenburg, Sweden*
[f] *Norwegian University of Life Sciences, Ås, Norway*
[g] *Department of Physics and Physical Oceanography, Memorial University of Newfoundland, St. John's, Canada*

## ARTICLE INFO

## ABSTRACT

In Fennoscandia, tectonics, Glacial Isostatic Adjustment (GIA), and climatic changes cause ongoing crustal deformation of some millimetres per year, both vertically and horizontally. These displacements of the Earth can be measured to a high degree of precision using a Global Navigation Satellite System (GNSS). Since about three decades, this is the major goal of the Baseline Inferences for Fennoscandian Rebound, Sea-level, and Tectonics (BIFROST) project.

We present a new velocity field for an extended BIFROST GNSS network in the ITRF2008 reference frame making use of the GNSS processing package GPS Analysis Software of MIT (GAMIT). Compared to earlier publications, we have almost doubled the number of stations in our analysis and increased the observation time span, thereby avoiding the early years of the network with many instrument changes. We also provide modelled vertical deformation rates from contributing processes, i.e. elastic deformation due to global atmospheric and non-tidal ocean loading, ice mass and hydrological changes as well as GIA. These values for the vertical component can be used for removal of these contributions so that the residual uplift signal can be further analysed, e.g., in the context of local or regional deformation processes or large-scale but low-magnitude geodynamics.

The velocity field has an uplift maximum of 10.3 mm/yr in northern Sweden west of the Gulf of Bothnia and subsidence exceeding 1 mm/yr in northern Central Europe. The horizontal velocity field is dominated by plate motion of more than 20.0 mm/yr from south-west to north-east. The elastic uplift signal sums up to 0.7–0.8 mm/yr for most stations in Northern Europe. Hence, the maximum uplift related to the past glaciation is ca. 9.6 mm/yr. The residual uplift signal after removal of the elastic and GIA contribution may point to possible improvements of the GIA model, but may also indicate regional tectonic and erosional processes as well as local deformation effects. We show an example of such residual signal discussing potential areas of interest for further studies.

## 1. Introduction

Fennoscandia, i.e. the geographic area of Norway, Sweden, Finland and parts of northwestern Russia such as Kola Peninsula and Karelia, forms the northwestern part of the Eurasian lithospheric plate. Its tectonic setting consists of, from west to east, the passive continental margin of the North Atlantic Ocean along Norway, the Caledonian mountain range in Norway and Sweden and the continental intraplate region of the East European Craton (Gregersen et al., 2021). Several deformation zones, mainly through Denmark and the southern Baltic Sea and summarized as the Trans-European Suture Zone (TESZ), separate Fennoscandia geologically from the rest of Europe to the south (e.g., Gregersen et al., 2002; Mazur et al., 2015; Artemieva, 2019).

Major faults on- and off-shore Western Norway (Sigmond, 2002) – in addition to major oceanic transform faults – are evidence of the Cenozoic opening and the spreading of the North Atlantic Ocean since ca.
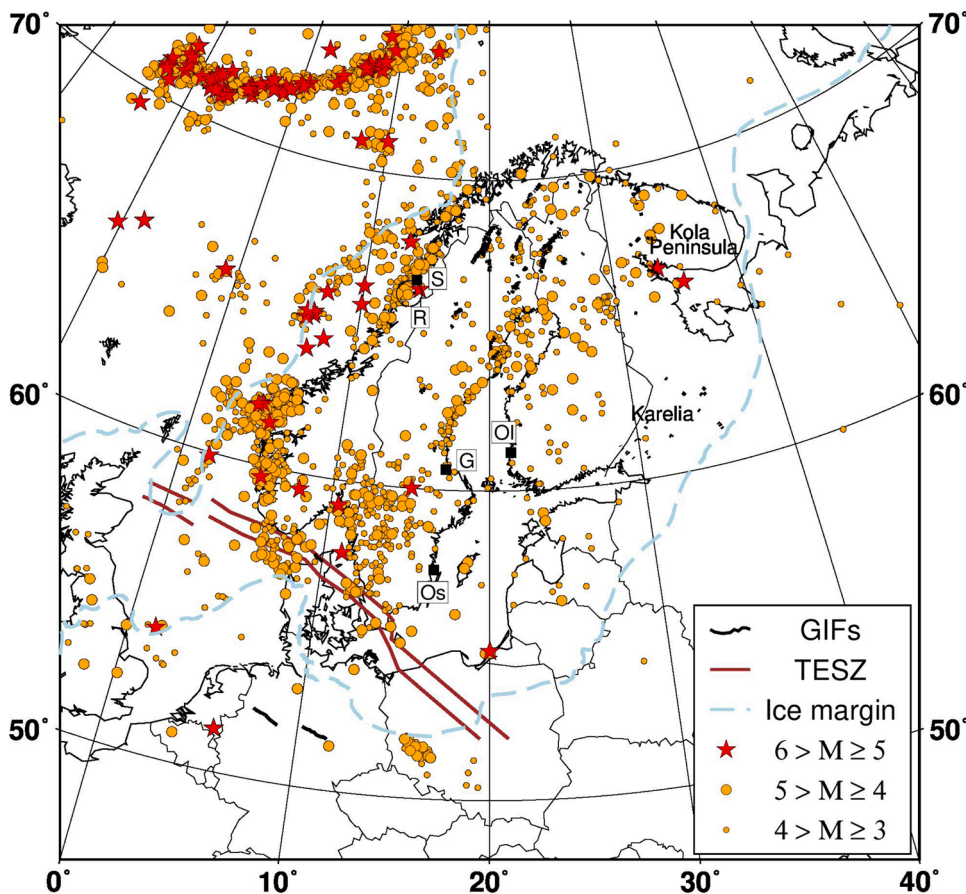
---

**Fig. 1.** Overview of Fennoscandian seismicity and names of locations mentioned in the text. Earthquakes (orange circles and red stars) above magnitude 3 are based on the Fennoscandian Earthquake Catalogue (FENCAT, 2020). The dashed blue lines show the ice margin at last glacial maximum according to Hughes et al. (2016). Brown lines sketch the location of the northern branches of the Trans-European Suture Zone (TESZ) according to Gregersen et al. (2002). Black lines mark the location of glacially induced faults (Munier et al., 2020). G = Gävle, Ol = Olkiluoto, Os = Oskarshamn, R = Ranafjord, S = Storglomvatnet. The Ranafjord area is encircled.

60 Ma ago (see e.g., Torsvik et al., 2002), which is the most recent major tectonic event that affected Fennoscandia. The North Atlantic ridge push force together with forces from the African-European collision initiated complex compressional and extensional evolution leading to a multitude of deformation zones, faults and fractures in all parts of Fennoscandia (Gregersen et al., 2021). Hence, some regions stick out in geoscientific investigations as behaving in a different manner than surrounding areas. An example is southern Norway, which has experienced fast recent uplift perhaps caused or facilitated by removal of the basal part of the cratonic lithosphere mantle (Artemieva, 2019).

Certainly the dominant and most well-known geodynamic process associated with Fennoscandia is the still ongoing land uplift. An ice sheet of ca. 3 km thickness at the peak of the last glaciation ca. 20,000 years ago depressed the lithosphere into the viscoelastic mantle. During and after deglaciation, the Earth surface undergoes time-delayed rebound towards an equilibrium state. This process of glacial isostatic adjustment (GIA) is well documented (Ekman, 2009; Steffen and Wu, 2011) and also has a lasting effect on sea-level changes today.

Despite the ongoing deformation mentioned above, Fennoscandia is considered as a typical low seismicity region. Nonetheless, some large earthquake events (magnitude 5 and higher, see Fig. 1) have been documented (Gregersen et al., 2021). In view of this, it is interesting to note that more than a dozen fault scarps some kilometre in length have been identified in northern Fennoscandia (see Fig. 1; Lagerbäck and Sundh, 2008; Munier et al., 2020) which show frequent seismic activity in the subsurface (Lindblom et al., 2015), but are apparently not accompanied with motion at the surface (Mantovani and Scherneck, 2013). These faults are known as postglacial or glacially induced faults (GIFs) and thought to have been reactivated at the end of the last glaciation that ended ca. 10,000 years ago (Steffen et al., 2021). They are thus considered to be a legacy of GIA. However, recent investigations

point to several phases of activity (Ojala et al., 2018), some as young as only 600 years ago (Olesen et al., 2021a), and therefore the interaction of GIA and intraplate seismicity requires further investigation (Olesen et al., 2021b).

Analysis of the processes mentioned above (including plate tectonics, GIA, earthquakes) is facilitated by Global Navigation Satellite Systems (GNSS) such as the Global Positioning System (GPS). In Fennoscandia, dedicated studies with continuous GNSS, largely within a GIA focus, have been pursued for about three decades (Milne et al., 2001; Johansson et al., 2002; Lidberg et al., 2007, 2010; Kierulf et al., 2003, 2013, 2014; Lahtinen et al., 2019). Much of this work has been completed under the BIFROST project (Scherneck et al., 2002). Growing lengths of time-series data and ongoing additions to the number of stations both improve collective signal quality (see e.g., Fig. 7 in Steffen and Wu, 2011).

Various regional and local GNSS studies have been performed. Kierulf (2017), for example, investigated neotectonics in Northern Norway with a combination of continuous and campaign GNSS. He found that the Ranafjord area is undergoing east-west crustal spreading and that the uplift gradient is larger than predicted with commonly used GIA models. Sjöberg et al. (2004) investigated in several campaigns (3 times a year) the 15 km × 20 km Äspö GPS deformation network in south-eastern Sweden, which surrounded the Oskarshamn nuclear power plant, with the goal to detect any crustal deformation exceeding (locally) 1 mm/yr after a few years of repeated observations. Similarly, Nyberg et al. (2013) investigated the area around the Olkiluoto nuclear waste disposal site in Finland with data from biannual GNSS campaigns. Both studies showed quite stable conditions at both sites.

The vertical velocity component of Fennoscandian GNSS networks shows a pattern of crustal uplift with the highest rates (∼ 1 cm/yr in Gulf of Bothnia) generally located in areas of thickest ice during the last
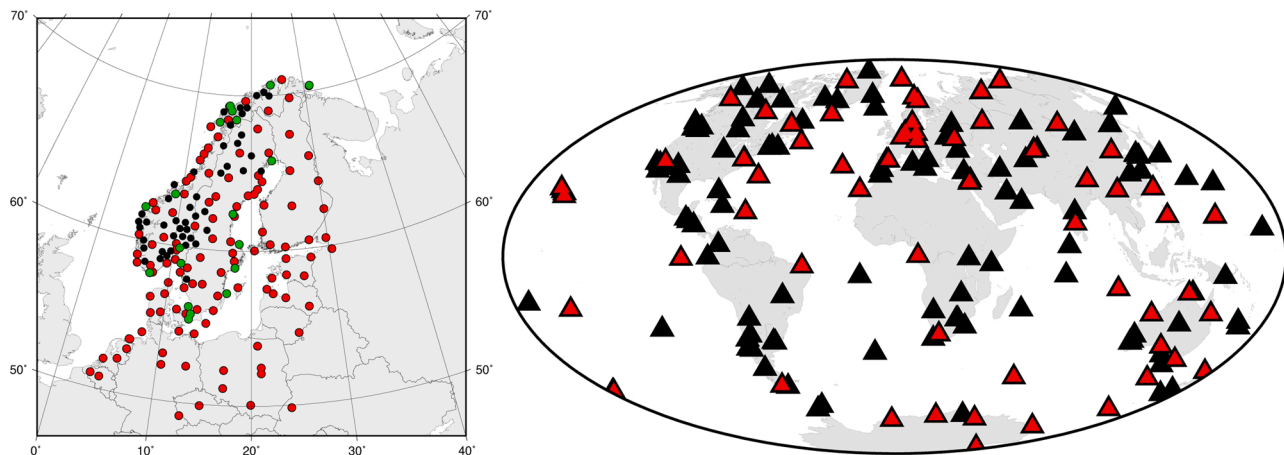
**Fig. 2.** The BIFROST2015 network and the global IGS network used in this study. *The stations marked with red circles represent the core Scandinavian network; these stations are mounted on a steel mast or concrete pillar anchored into crystalline bedrock. Stations marked with black or green circles are stations not properly mounted to bedrock, but appear as stable and are either filling important gaps in the network (black) or co-located with tide gauges or absolute gravity points (green). Black and red triangles are the global stations used in the GAMIT analysis, the black triangles are the stations used in the global reference frame realization.*

glacial period ($\sim 3,000 \, \mathrm{m} \sim 20,000$ years ago). This rate of uplift gradually decreases with distance from this maximum. In the so-called forebulge area, i.e. Belgium, the Netherlands, Central Germany, central Poland, south-eastern Lithuania, Belarus and western Russia, the crust is undergoing a small subsidence (Steffen and Wu, 2011; Bogusz et al., 2019). Horizontally, the velocities show north-eastward plate motion of the Eurasian plate. Transformed into a frame that fits the GIA process, the crust is undergoing an outward movement from this maximum to the so-called axis of tilting or zero line or hinge line (the area of no vertical movement) with largest values in mid-distance. This velocity field pattern is typical for a region where an ice sheet has vanished some five to ten thousand years ago, as has been shown with GNSS in North America (e.g., Sella et al., 2007; Simon et al., 2016; Robin et al., 2020).

Because of the clear GIA signature, BIFROST results have been used in GIA modelling to identify best-fitting earth models (assuming that the ice sheet chronology is described adequately with a dedicated model) (e. g., Milne et al., 2001, 2004; Steffen and Kaufmann, 2005; Zhao et al., 2012; Kollo et al., 2016). This in turn contributes to the selection of optimal locations for new GNSS stations (Wu et al., 2010). Other applications include the comparison with results of the Gravity Recovery and Climate Experiment (GRACE) twin-satellite mission (e.g., Steffen et al., 2010; van der Wal et al., 2011), the development of land-uplift models (Ågren and Svensson, 2007; Hill et al., 2010; Müller et al., 2012; Simon et al., 2018), stress and strain analysis (Keiding et al., 2015; Gradmann et al., 2018), as correction of the vertical land motion in sea-level studies (e.g., Santamaría-Gómez et al., 2014), and to determine the $\dot{g}/\dot{h}$-ratio in Fennoscandia by comparison to absolute gravity measurements (e.g., Olsson et al., 2019; Bilker-Koivula et al., 2021).

Although many velocity fields for Fennoscandia have been published over the last two decades, the last one under the umbrella of the BIFROST project was provided by Lidberg et al. (2010). The aim of this paper is to provide a new quality-assessed BIFROST velocity field from a densified network of GNSS stations with uncertainties, and additionally model-based GIA and elastic corrections for these Fennoscandian, Baltic and northern Central European stations. The velocities are meant to be used for geoscientific studies on GIA, climate change, neotectonics and/or hydrological loading.

The number of stations is increased from a bit more than 80 in Lidberg et al. (2010) to 164. Especially in Fennoscandia, much more stations are part of our velocity field than in the dataset provided by the Nevada Geodetic Laboratory at the University of Nevada, Reno, which was used, for example, in the generation of the global GIA GPS data set of Schumacher et al. (2018) or in a global analysis of the contemporary

mass change effects on sea-level changes and vertical land motion by Frederikse et al. (2019). For interested users, we add vertical velocities for GNSS stations close to other geodetic infrastructure like tide gauges and absolute and superconducting gravity stations to the network. Compared to previous BIFROST studies, we densify the network especially in Norway, Estonia and Latvia.

One must further note that ongoing ice melt as observed in Greenland, Antarctica and smaller glaciers around the world causes a near instantaneous (elastic) response of the crust (Frederikse et al., 2016). The melting rates are nowadays so large that the combined effects can easily exceed 0.5 mm/yr in the vertical component of GNSS measurements some thousand kilometres away of the source (Simon et al., 2018; Frederikse et al., 2019; Ludwigsen et al., 2020), thus the typical GIA pattern in Fennoscandia is slightly altered. Hence, these effects should be removed before, for example, earth rheology can be determined with commonly used GIA models. We provide elastic corrections for each station due to Atmospheric (ATM) and Non-Tidal Ocean (NTO) loading, recent ice melt of major ice sheets and glaciers as well as hydrological changes dependent on the observational time span of each station. We also add values from a standard but well-fitting GIA model that is in line with previous results for readers that wish to investigate regional or local deformation signals and thus need a GIA signal correction. Finally, we compare our residual signal after removal of the elastic and GIA contributions to the global residual uplift signal provided by Frederikse et al. (2019).

## 2. GNSS data processing

The stations are plotted in Fig. 2. We name this set of stations the BIFROST2015 network. These are the same stations listed in Vestøl et al. (2019) except (i) those rejected by Vestøl et al. (2019) (DONC, HELC, LILC, PREI, ROAC, TEJH, TNSC) and (ii) those that after further analysis have shown anomalous behaviour (large residuals, motion in other direction than surrounding stations) in one of the horizontal components (FLIC, HAMC, HELG, KOSG, NARC, OPEC, STL0, VIKC). We also analysed around 150 global International GNSS Service (IGS) stations from the IGb08 Core Reference Frame sites (Fig. 2, right). These stations ensure a good connection to the International Terrestrial Reference Frame (ITRF2008).

The derived GNSS station velocities, presented in the supplementary information, are based on available data for the Nordic area from the period January 1, 1997 to December 31, 2014. Due to a number of instrument upgrades and changes at the stations in the first three years of our processing time span that may have affected our velocity estimates
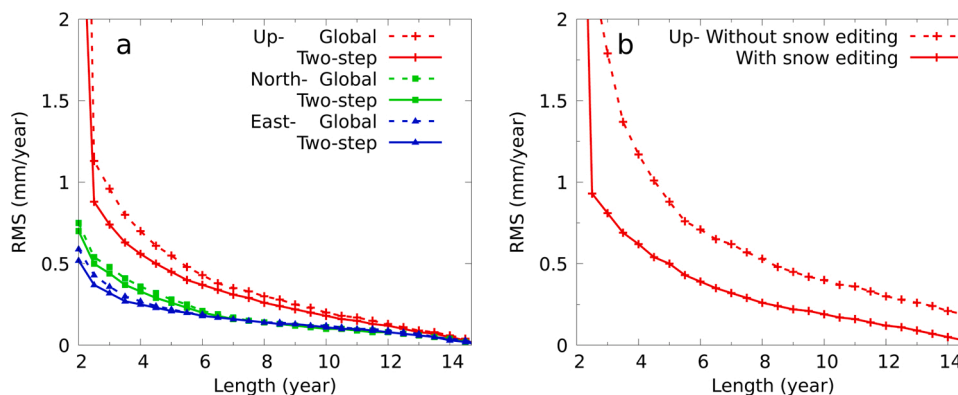
**Fig. 3.** Convergence plot of velocity estimates. (a) Shows the convergence for the global solution (dashed lines) vs. the solution using the two-step approach (solid lines). The blue, green and red curves are the east, north and height component, respectively. (b) Shows convergence for stations affected by snow. The solid red curve is based on rate estimates using the extra snow iteration to remove outliers. The dashed curve is based on rate estimates with ordinary outlier removal.

negatively, we decided to provide the velocity field for the period 2000.0 to 2015.0. The solution has been processed in early 2015 and thus included at that time all data available. As part of projects of the Nordic Geodetic Commission (NKG), it was then used for development of a land uplift model (NKG2016LU, Vestøl et al., 2019) and a velocity field model (NKG_RF19vel, Häkli et al., 2019). These models are official models to be used at Nordic national mapping authorities, e.g., for national reference frame solutions.

In the following, we describe briefly the processing where we compare time-series analysis methods. Special attention is paid to the reference frame realizations and how to develop a global reference frame with maximal regional consistency. In order to assess the effects of snow and ice on the time series, an extra iteration is performed in the time-series analysis to remove data points biased by snow on the antenna. The stability of velocity estimates are examined with a convergence analysis. Detailed information on some of the processing steps can be found in the appendix.

We have used the geodetic GPS software package GAMIT (King and Bock, 2003; Herring et al., 2015). The atmospheric zenith delay was estimated with a 2-hourly piece-wise linear model together with a daily troposphere gradient. We have used 10-degree cut-of-elevation, the igs08.atx antenna phase center model, the Vienna Mapping Functions (VMF1) (Boehm et al., 2006) tropospheric mapping function and the FES2004 ocean loading model (Scherneck, 1991; Lyard et al., 2006). Atmospheric tidal loading is included, but not any model for the non-tidal atmospheric loading, nor a model for higher order ionosphere disturbances.

The stations are divided in subnetworks of stations in Finland, Sweden, Norway, the Baltic countries, Denmark and northern Central Europe, and several densification networks in Norway and Sweden (see Fig. 2). Additionally, approximately 150 global IGS stations were divided in three subnetworks. The different subnetworks were analysed on a daily basis and merged to one combined network including global and regional stations for each day using Global Kalman filter VLBI and GPS analysis program (GLOBK) (Herring et al., 2015). This ensures a good connection to the global reference frame. The results are given in IGb08 realized in a two-step procedure described in Appendix A. The effect of the two-step approach on the rate estimates is included in Section 2.2.

### 2.1. Time-series analysis

The time series are analysed assuming a combination of white noise and power-law noise where also the spectral index was estimated. In addition, offsets for all antenna and radome changes were included in the time-series analysis as well as offsets where breaks in the time series were obvious after a visual inspection. Outliers were removed in a

preliminary analysis using an in-house least-squares adjustment program, before applying the time-series analysis with the Cheetah software (see below). Outliers were removed based on a $3\sigma$-criteria. For stations heavily affected by snow the time series were cleaned in an extra iteration (see Appendix B). The effect of the extra snow iteration on the rate estimates is included in Section 2.2.

We used the software Cheetah (successor of the CATS software, Williams, 2008) in the time-series analysis. Cheetah makes use of the differencing approach described in Bos et al. (2008). The great advantage is a significantly reduced time consumption: while calculations with CATS can take hours Cheetah runs within minutes. However, Cheetah does not include the daily position uncertainties in the time-series analysis while CATS does.

In Appendix C results from time-series analysis using different software and noise models are presented and discussed. Generally, choosing another software or noise model results in only very small differences in rate estimates. For most stations, a combination of white noise and power law noise gave lower uncertainties than assuming white noise and flicker noise.

### 2.2. Convergence analysis

To examine the stability of our velocity estimates, we have performed a convergence analysis using solutions from stations established in year 2000 or earlier. Velocities have been computed for each time series, first using only the last 2.5 years of data, then the last 3.0 years of data and then extending the time period by 0.5 years until 15 years of data have been included. The RMS of the differences between the velocities for the shorter period and the velocities for the complete time series (back to 2000-01-01) is calculated for each time span and component:

$$\text{RMS}(\Delta t) = \sqrt{\sum_{i=1}^{n} \frac{(r_i(\Delta t) - \overline{r_i})^2}{n}}, \tag{1}$$

where $r_i(\Delta t)$ is the rate for station $i$ with time series of length $\Delta t$. $\overline{r_i}$ is the rate for station $i$ using the complete time series back to 2000-01-01 and $n$ is the number of stations. This test gives a measure of the stability of the estimated secular rates as function of time-series length.

The results are plotted in Fig. 3a, both for the global solution and the solution using the two-step approach described in Appendix A. We see a clear improvement using the two-step approach especially in the vertical component. For example, for a precision of less than 0.5 mm/yr, 4.5 years are sufficient with the two-step approach while approximately 5.5 years are necessary using the traditional one-step global realization.

GNSS stations in a region can have a spatially correlated signal, so-called Common Mode (CM)-signal (Wdowinski et al., 1997). The
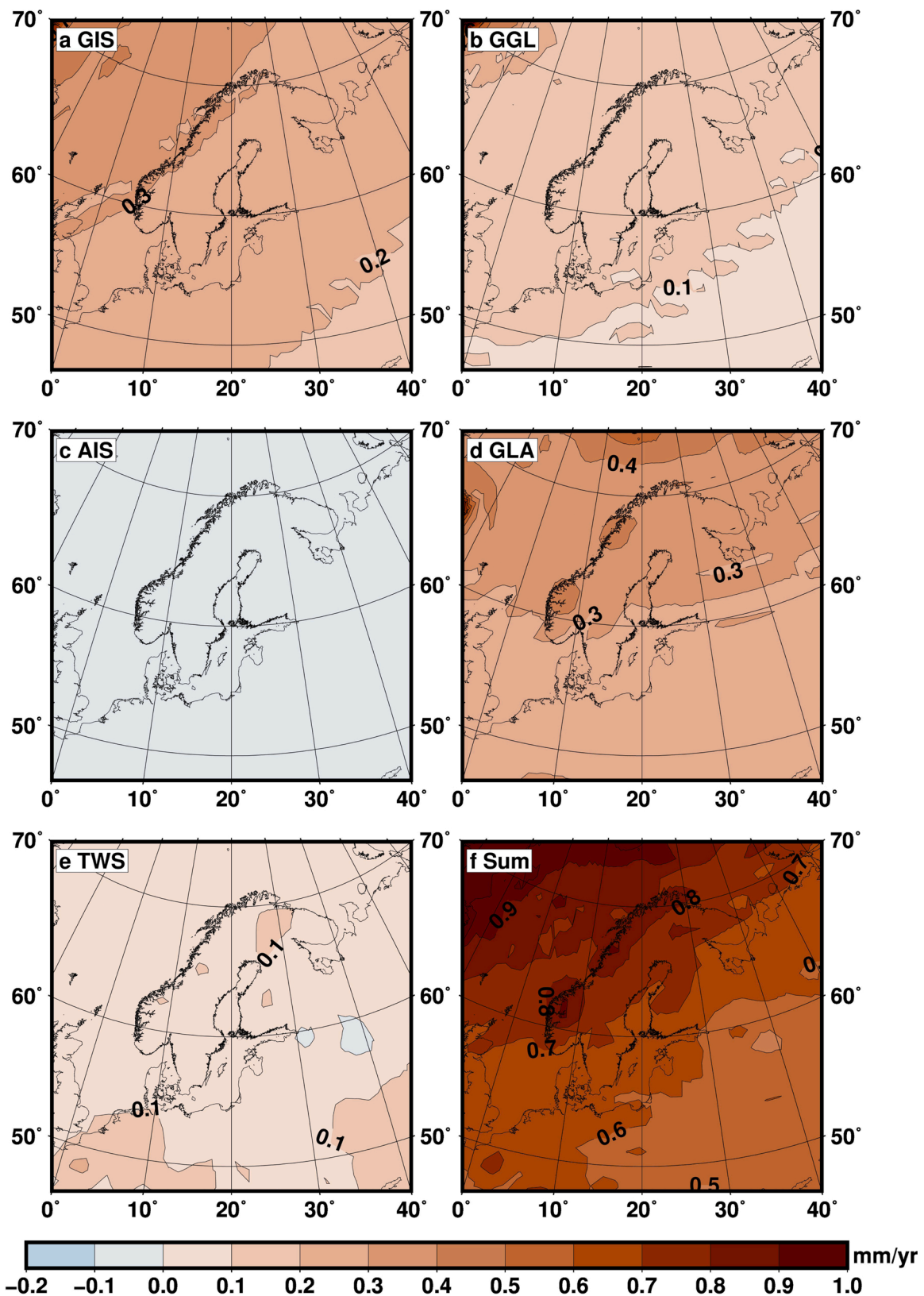
**Fig. 4.** Elastic effect in Northern Europe due to 2000.0–2015.0 mass changes of (a) the Greenland Ice Sheet (GIS), (b) Greenland glaciers (GGL), (c) the Antarctic Ice Sheet (AIS), (d) global glacier model (GLA), (e) hydrology model (TWS) and (f) the sum of (a) to (e). Unit is mm/yr.

removal of the CM-signal can reduce noise in time series. The CM-signal could come from the GNSS analysis strategy and from the strategy for reference frame realisation. It could come from mismodelled orbit, clocks or Earth orientation parameters, or unmodelled large-scale hydrology or atmospheric effects. These biases influence the rates estimates especially for shorter time series. The two-step solution removes the CM-signal.

A convergence analysis for the stations affected by snow is included in Fig. 3b. The effect of the extra iteration described in Appendix B is clearly visible. With the standard time-series analysis, the stations affected by snow need more than eight years to achieve a precision of 0.5 mm/yr. After using the extra snow iteration these stations give results at about the same level as the rest of the network, i.e. ca. five years of observations are needed.

Note that these convergence results are relative to the rate for the complete time series of 15 years. To get the uncertainty, the precision from the convergence analysis has to be added in quadrature (square root of the sum of squares) to the uncertainties from the complete time series of 15 years. The mean rate uncertainties for the time series of 15 years are 0.05 mm/yr, 0.05 mm/yr and 0.12 mm/yr, in the east, north and height component, respectively.

## 3. Global elastic component for the correction of uplift rates

Dynamic processes such as ice melt and hydrological changes as well as ATM and NTO loading can induce instantaneous deformations (e.g., Dobslaw and Thomas, 2007; Compton et al., 2017). Most notably, ice melt and hydrological changes can affect vertical rates (e.g., Argus et al., 2014; Frederikse et al., 2016, 2019). We consider elastic responses during our observation time span from 2000.0 to 2015.0 and provide corrections for elastic effects due to ATM loading, NTO loading, and loading from changes in hydrology and ice masses for each station in the table in the supplementary information.

The ATM and NTO loading signals are downloaded from http://massloading.net/ (Petrov and Boy, 2004). The NTO signals are calculated using model MPIOM06 (Dobslaw and Thomas, 2007) and the ATM signals with model GEOS-FPIT provided by the Global Modeling and Assimilation Office (GMAO) at NASA Goddard Space Flight Center.

The elastic displacement caused by recent ice melt in Antarctica, Greenland, and global glaciers as well as terrestrial water storage changes is computed based on results derived within the framework ESA CCI project Sea Level Budget Closure (SLBC) (https://climate.esa.int/en/projects/sea-level-budget-closure, Horwath et al., 2020). Four main contributions are provided as time series of global monthly gridded values with a nominal resolution between $0.5 \times 0.5$ and $1 \times 1$ degrees:

1. TWS (Terrestrial Water Storage from the WaterGAP Global Hydrological Model (WGHM), Cáceres et al., 2020; Döll et al., 2003; Müller Schmied et al., 2016): time series over the period 1992–2016 of global gridded data (nominal resolution of 0.5 degree) for four different models in terms of water surface density variation (in mm/yr) for each cell. The four models are different in terms of irrigation (optimal and 70%) and the forcing method (GPCC monthly vs. CRU TS 3.23 monthly precipitation sums) (see e.g., Cáceres et al., 2020). We used the average according to recommendation in the SLBC project (Horwath et al., 2020).
2. GLA (Glaciers from the Open Global Glacier Model (OGGM, Maussion et al., 2019)): monthly time series over the period 1992–2016 of global gridded data (nominal resolution of 0.5 degree) of one model in terms of mass (in Gt) for each cell.
3. AIS (Antarctic Ice Sheet mass changes from the Gravimetric Mass Balance product – AIS_GMB): time series over the period 2002–2016 of grids (nominal resolution of 1 degree) for the mass changes in terms of surface density ($kg/m^2$) derived from GRACE.
4. GIS (Greenland Ice Sheet mass changes derived from radar altimetry): monthly time series over the period 1992–2016 of grids

(nominal resolution of 1 degree) for the trend of mass changes in terms of mass rate (Gt/yr) (Simonsen et al., 2021).

For more information on each product we refer the reader to the corresponding paper.

We converted the gridded data into spherical harmonics (SH) up to maximum degree and order 128. The mass lost by the global land water storage (TWS, ice sheets and glaciers) can be quantified in terms of sea-level equivalent, by assuming, as a starting guess, that the water is spread uniformly across the ocean surface. The mass that is redistributed from the land into the ocean produces a deformation in the gravity field (e.g., Farrell and Clark, 1976), which in turn produces a non-uniform distribution of the water in the ocean. So, in order to properly compute the actual deformation caused by the global changes in the total land water storage we account for its related relative sea-level change. This was done with the code TSec v4, benchmarked in Martinec et al. (2018).

From the resulting deformation we extracted the global uplift deformation field only, with a resolution of about 1 degree. Subsequently, we extracted interpolated values at the position of the GPS stations for the observation time span of each individual GPS station. This information is added for each contribution in the table in the supplementary information. An example for the elastic contribution from 2000.0 to 2015.0 is shown in Fig. 4.

The error of the elastic contribution can be estimated to be at most 10%. In fact, it is directly related to the total error of the mass loading, which has been computed in the SLBC project (see p. 74 in Horwath et al., 2020). The total mass for the sea-level budget has a total error smaller than 10%. Moreover, the near-field contribution (Scandinavian glaciers and hydrology) to the elastic uplift is minor with respect to the far field contribution (see also Ludwigsen et al., 2020). So, the error on the total mass for the sea-level budget is reflected in the elastic uplift rate.

We do not provide a correction for the horizontal velocities as this elastic signal can be considered very small (a factor of 3–4 smaller than the vertical component, Samrat et al., 2020) and homogeneous over whole Fennoscandia, so that it is removed in a reference frame transformation.

## 4. Glacial isostatic adjustment model and reference frame

A GIA model provides the estimated deformation response of the solid Earth to past changes in surface loading from ice and ocean, through a mathematical combination of an ice-sheet history model with a model describing the interior of the Earth with a set of geometric and rheological parameters. Velocity fields of formerly glaciated areas show a clear sign of GIA (Milne et al., 2001) and they can serve two purposes: First, an ice and rheological model combination can be identified by determining the best fit of the velocities calculated with GIA models to the observations. Second, the velocity field of a GIA model, in turn, can be removed from an observed velocity field to investigate other velocity field contributions, e.g., in sea-level studies. As an example, we use a GIA model based on typically used earth structure in such investigations that fits the 3D velocity field of BIFROST2015 well. We do not perform a search for the best-fitting GIA model in this study as we would like to leave this to the interested community. With the help of our GIA model example we can demonstrate a brief geodynamic analysis of the residual velocity field after removal of the GIA signal from our velocity field.

A key issue is that ITRF2008 is not appropriate for a comparison of the velocity field to the GIA model. One has to remove the plate-tectonic signal before comparing the horizontal velocities. Depending on the chosen method, this can also affect the vertical component. Johansson et al. (2002), Kierulf et al. (2003, 2013), Lidberg et al. (2007), and Hill et al. (2010) use different strategies to remove the tectonic signal before comparison of the observed velocities with the GIA models. Furthermore the definition of geocenter and scale might skew the comparison
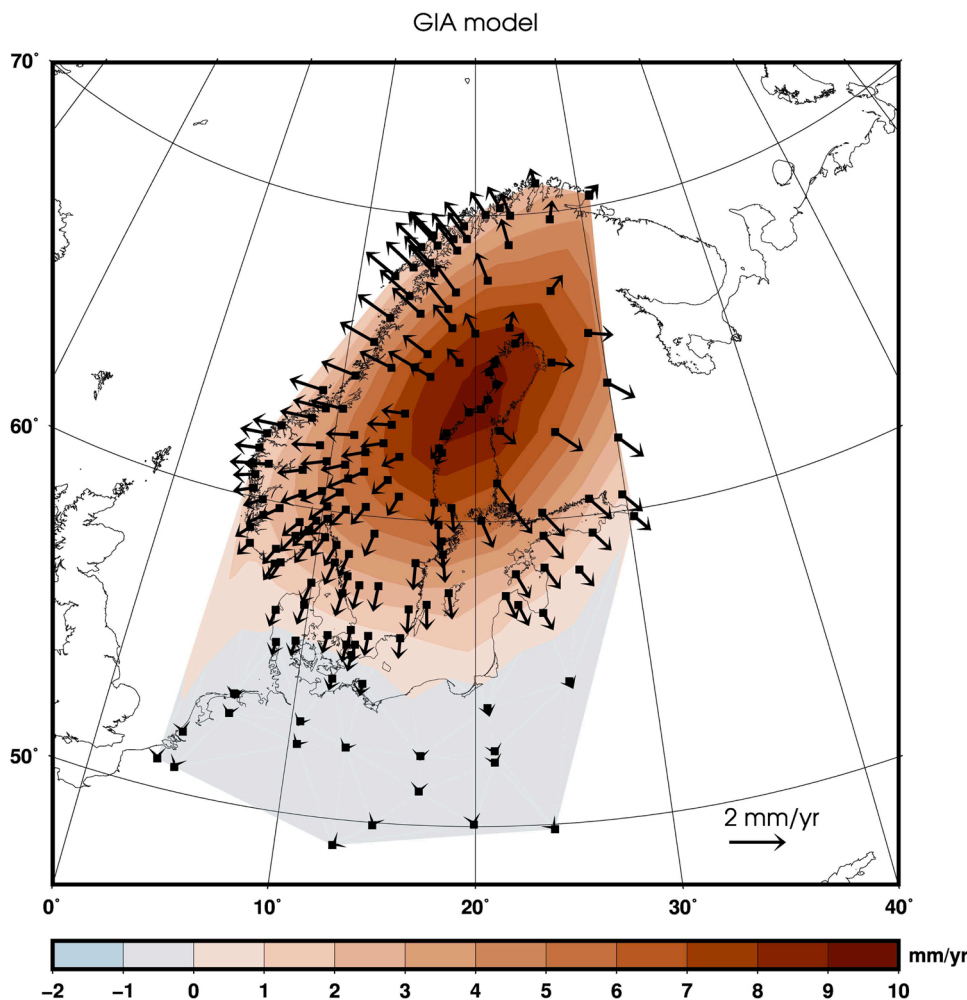
**Fig. 5.** Three-dimensional velocity field [mm/yr] in Northern Europe from our selected GIA model example, plotted at the location of the GNSS stations. The contours are drawn with Delauney triangulation of the GMT5 software.

between observations and models. In Kierulf et al. (2014) a new approach named the GIA-frame approach was introduced to avoid the problem of plate-tectonic impacts on reference frames in the comparison between observations and GIA models. The core idea is to realize the velocity field in the reference frame implicitly given by the GIA model under consideration, see Appendix D for details.

For calculation of the velocities from our GIA model, we use the software ICEAGE (Kaufmann, 2004) that is based on the viscoelastic normal-mode method (Peltier, 1974). It applies a pseudo-spectral approach with a spherical harmonic expansion in the spectral domain truncated at degree 192 (Steffen and Kaufmann, 2005). This results in approximately a 1-degree spatial resolution. Details on the theory implemented in ICEAGE can be found in Kaufmann and Lambeck (2000) and Kaufmann and Lambeck (2002). The software has been successfully applied since the mid-1990s in more than two dozen studies (e.g., Kaufmann and Lambeck, 1997; Kaufmann, 2000; Steffen and Kaufmann, 2005; Steffen et al., 2010; Kierulf et al., 2014; Olsson et al., 2019; Vestøl et al., 2019).

The GIA model consists of a so-called three-layer one-dimensional (1D) compressible, Maxwell-viscoelastic Earth model with a lithospheric thickness of 120 km, an upper-mantle viscosity of $7 \times 10^{20}$ Pa s, and a lower-mantle viscosity of $2 \times 10^{21}$ Pa s. The Earth model parameters are in line with previous findings using solely GNSS results for Fennoscandia (see e.g., Milne et al., 2001, 2004; Steffen and Kaufmann, 2005; Bergstrand et al., 2005; Zhao et al., 2012; Kierulf et al., 2014; Schmidt et al., 2014), which showed lithospheric thickness of

93–160 km (with majority pointing to 120 km), upper-mantle viscosity in a range of (3.4–10) $\times 10^{20}$ Pa s, and lower-mantle viscosity of at least $2 \times 10^{21}$ Pa s. However, our chosen values may differ to those of GIA models that rely on either geological data (Lambeck et al., 1998, thinner lithosphere and weaker upper-mantle viscosity) or GRACE data (Steffen et al., 2010, thicker lithosphere and weaker upper-mantle viscosity). Note that the results are subject to the applied model of ice load history. Most previous studies use either a version of ANU-ICE (also called RSES) from the group of Kurt Lambeck or a model of the ICE-xG series from the group of Dick Peltier.

For ice load history, we use the GLAC1-D Eurasian ice component model 90227, which is the preferred GLAC ice model for Northern Europe as it minimizes the collective misfit to a set of observational constraints, including relative sea-level data, GNSS-derived uplift rates, geologically inferred ice margin location history, and the sea-level rise due to meltwater pulses (Tarasov et al., 2012; Tarasov, 2013; Root et al., 2015; Nordman et al., 2015). From this GIA model, we then calculate the absolute velocity in three dimensions ({N, E, U}_GIA in the table of the supplementary material) for each GNSS station location. The corresponding velocity field is shown in Fig. 5.

The velrot program of GAMIT is used for transformation of the observed velocity field into the GIA frame of our selected GIA model. First, the vertical component of the observations is corrected for elastic effects. We then apply a rotation and translation with 50% weight on the vertical velocities. This transformation has been found appropriate in the development of the NKG_RF19vel deformation model for Northern
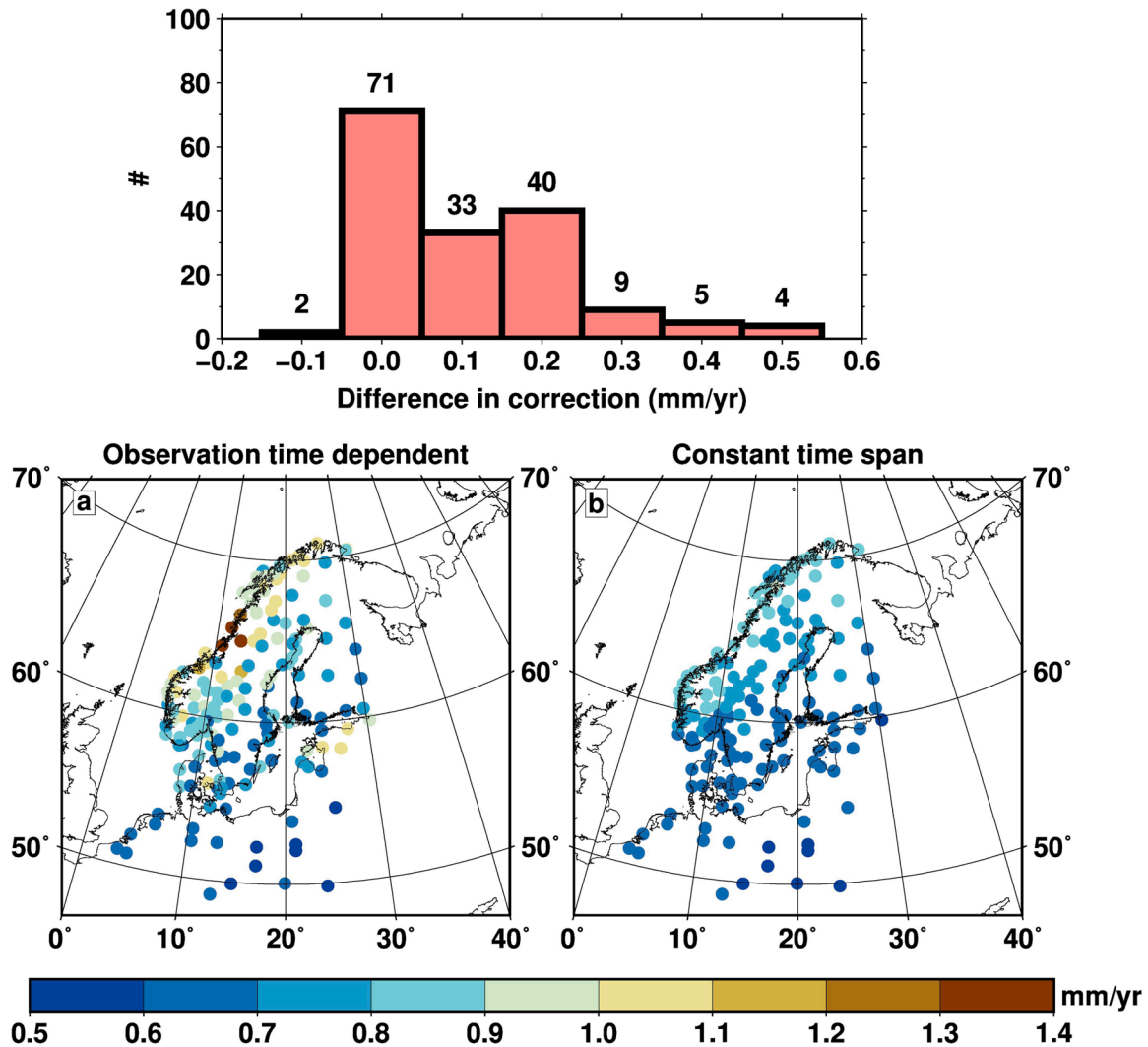
**Fig. 6.** Comparison of total elastic correction [mm/yr] if (a) calculated depending on the time span of observation of each station or (b) using a constant time span from 2000.0–2015.0. Difference in elastic correction for most stations (146 of 164, 89%) is within a 0.2 mm/yr level, see histogram atop.

Europe (Häkli et al., 2019).

The mean difference of our GIA model to the transformed and elastically corrected 3D velocity field is 0.26 (N) and 0.18 mm/yr (E) horizontally and 0.45 mm/yr vertically. Restricting to a subset of 34 long-term observing (up to 15 years) and very stable stations, the mean difference is 0.22 (N) and 0.15 mm/yr (E) horizontally and 0.32 mm/yr vertically.

## 5. Results and discussion

We separate this section into a discussion of our elastic correction including comparison to corrections provided in previous studies, the performance of our selected GIA model and a brief analysis of the residual velocity field after elastic and GIA correction.

### 5.1. The effect of elastic correction as a function of observation time span

Combined elastic effects are corrected as a function of the observation time span of each individual GNSS station. This is necessary because ice melt is not constant over time. For example, ice melt in Greenland and Svalbard was on average much larger in the late 2000s until 2015 than on average during the 15-years period from 2000.0–2015.0. Therefore, stations with a long observation time span, i.e. from 2000.0–2015.0, have on average smaller corrections than stations with a

short observation time span beginning in the late 2000s until 2014, see the table in the supplementary information.

We visualize this effect in Fig. 6 where we compare our correction depending on observation time span (a) with a constant time span (b). For the latter, the pattern of decreasing values from north to south is mirrored by results for the sum of effects (compare to Fig. 4f). A correction using observation time span shows isolated, mainly larger elastic correction. While the difference between these two approaches can be otherwise considered small (at most 0.2 mm/yr) for 89% of the stations, see histogram above, there are 18 stations with considerable time span effect up to a level of half a millimetre per year. This result contrasts with that of Schumacher et al. (2018), who found no significant time span effect for 98.9% of the stations used in their analysis with more than 3000 stations tested.

The elastic correction is at least 0.5 mm/yr at the GNSS stations considered (Figs. 6, Fig. 7 and supplementary information). For the majority of stations, the correction is mainly between 0.6 and 1.0 mm/yr. The largest elastic correction is 1.35 mm/yr for station ROYC. The uplift signals from ATM and NTO are generally very small for the complete time span of observations from the GNSS sites and often cancel each other, so that a combined contribution of larger than ±0.1 mm/yr is rare (only concerns stations BORJ, IRBE, NYB0, PULK, SASS, SIRC, SMID, SULD, TALS, TORX). The largest effect here is for station IRBE with 0.25 mm/yr. The AIS melting contributes negatively to the elastic
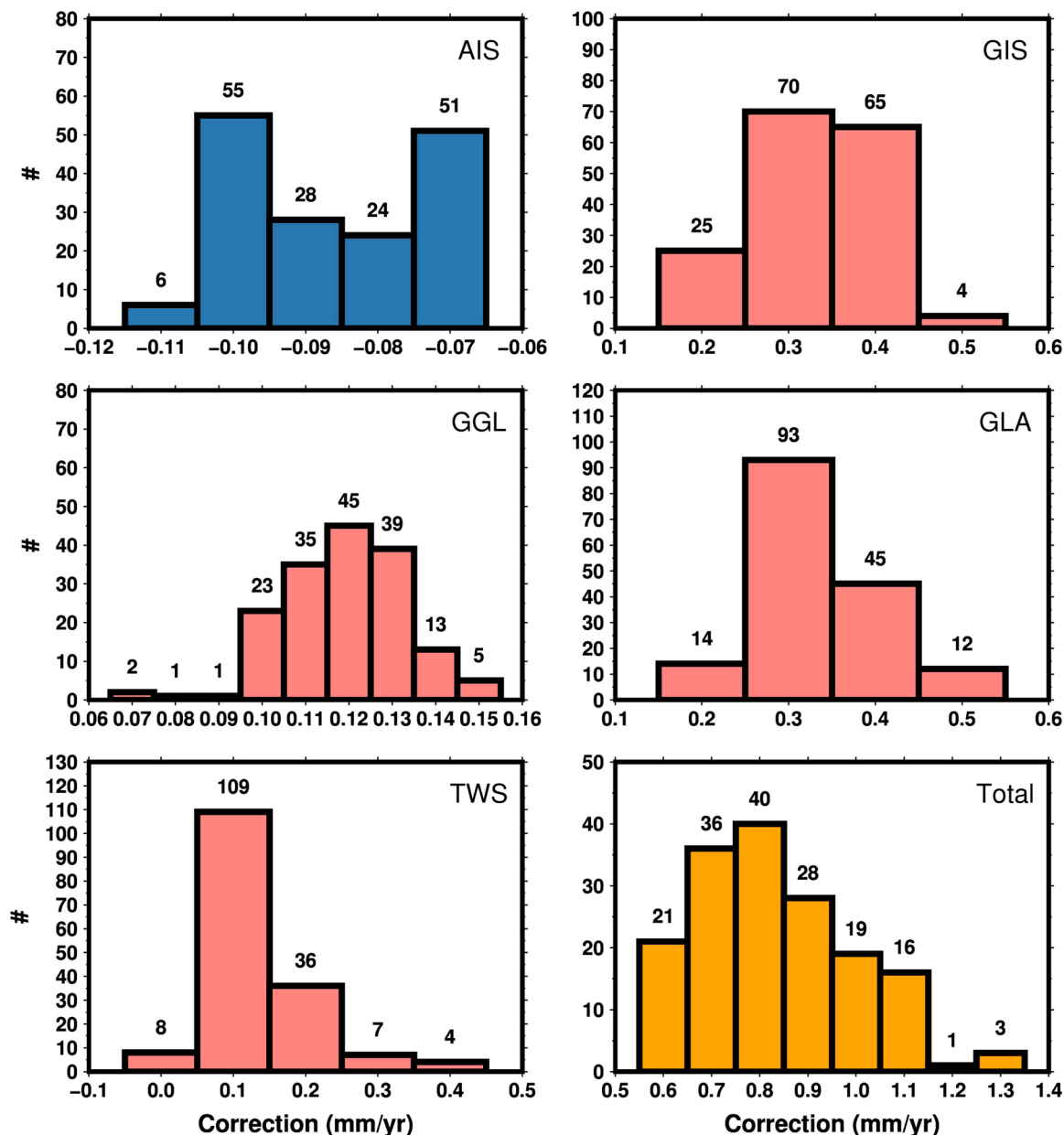
**Fig. 7.** Histogram of elastic contribution of each component (blue and red) at the GNSS stations and the total elastic correction (orange). AIS = Antarctic Ice Sheet, GIS = Greenland Ice Sheet, GGL = Greenland glaciers, GLA = global glacier model, TWS = terrestrial water storage from hydrology model. Note the different scales for each histogram.

budget with − 0.10–0.07 mm/yr, meaning its correction would increase the observed uplift. Correcting changes of the GIS and surrounding glaciers combined reduces the observed uplift instead with 0.3–0.6 mm/ yr. Correcting global glacier changes, where ice melt on Svalbard has the largest effect on Northern Europe (see Fig. 4), additionally reduces the observed uplift by ca. 0.2–0.5 mm/yr. Elastic correction due to hydrological changes strongly depends on the observation time span. The longer it is (i.e. larger than 10 years), the smaller is the correction, which is then less than 0.1 mm/yr and therefore almost negligible. For shorter time spans of only 5 or 6 years, elastic effects from hydrology of more than 0.4 mm/yr can result for some stations.

The magnitude of our elastic correction results agrees with most previous results. Simon et al. (2018) found an elastic contribution of 0.3–0.5 mm/yr for GNSS stations in Fennoscandia, with lower values in the south. However, their time span from 1993–2014 is much longer than ours and is not dependent on the observation time span of the stations. The elastic contribution in the 1990s is especially much smaller

than in more recent years, hence their average can be expected to be lower compared to our result. Their uncertainties for the elastic contribution are estimated to be less than 0.05 mm/yr, hence maximum 10% and thus in line with our estimated uncertainties.

Ludwigsen et al. (2020), providing a vertical land motion model for the wider Arctic, calculated a total elastic contribution from 2003–2015 of ca. 0.4 mm/yr in Denmark and 0.8 mm/yr in the northern parts of Fennoscandia, which are larger values than those of Simon et al. (2018) but, due to a comparable time span, much closer to our result. As in our result (see Fig. 4d), Ludwigsen et al. (2020) found a contribution of glacier retreat in the Norwegian mountains to be very local adding 0.1–0.2 mm/yr in the very near field.

Schumacher et al. (2018) used a time span from 2005–2014 for calculating an elastic correction, which is between 0.5 and 1 mm/yr in Fennoscandia (their Fig. 5) and thus agrees with our findings. They used and filtered stations from the Nevada Geodetic Laboratory (NGL) at the University of Nevada, Reno (UNR) (Blewitt et al., 2018). However, in the
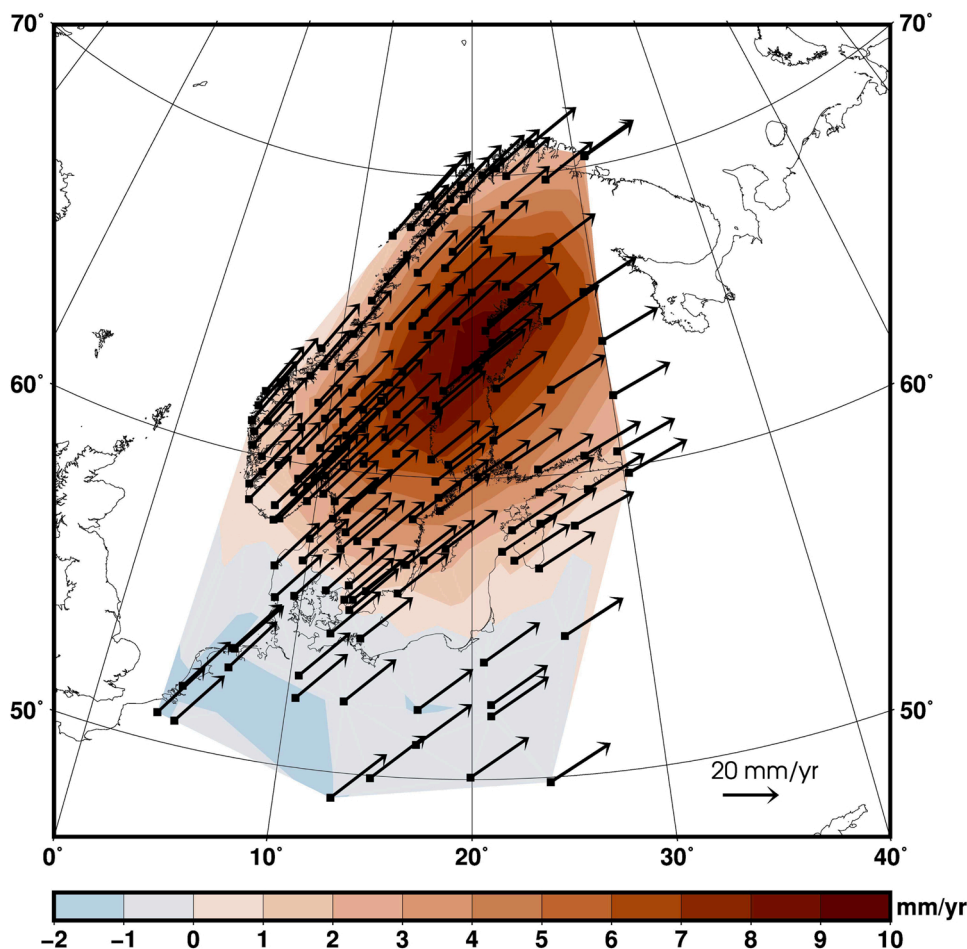
**Fig. 8.** BIFROST2015 velocity field in the ITRF2008 frame after elastic correction of the vertical component. Maximum uplift is a bit less than 10 mm/yr. Dominating plate motion from SW to NE is clearly visible in the horizontal components. Contours are drawn with Delauney triangulation of the GMT5 software.

Nordic countries the number of stations differs largely between their and our study, and also the time span among our stations differs significantly.

Frederikse et al. (2019) used a different approach to remove the elastic contribution from a global GNSS dataset (also from Blewitt et al., 2018) by converting the contemporary mass signal detected by GRACE from March 2002 to April 2017 into a vertical land motion signal. In Fennoscandia, this signal agrees with our results, again spanning between 0.5 and 1 mm/yr with lower values for southern stations and higher values for northern stations. Because of their different approach, their uncertainties are partly much larger (up to 50% in Fennoscandia, see their Fig. 8f) than our estimate (max 10% of the signal) or the values provided by Simon et al. (2018).

### 5.2. The GIA pattern of the last glaciation – indications on GNSS velocity field quality and GIA model fit

The elastically corrected (in the vertical component only) result is shown in Fig. 8. The typical elliptic uplift signature is still clearly visible. The maximum of ca. 9.6 mm/yr is along the northern Swedish coast of the Gulf of Bothnia. From here, uplift is decreasing gradually in all directions. The hinge line can be found south of the Norwegian coast, crossing the northern-most tip of Denmark, the Öresund area and south-western Sweden, touching the northern tip of Poland and then turning NE-ward to the Russian coast at the east of the Gulf of Finland. The forebulge, where the crust subsides, is only slightly traceable because station density is low. Subsidence of more than 1 mm/yr is observed for the Netherlands and western Central Germany. The zone of maximum

subsidence in the forebulge is about 300–500 km to the south of the hinge line. The horizontal velocity field exhibits the dominating plate-motion pattern from the SW to the NE with values of more than 20 mm/yr.

Our maximum uplift of ca. 9.6 mm/yr is observed at the stations UME0 in Umeå and SKE0 in Skellefteå. This is much lower than the values of 10.3 (SKE0), 14.1 (SKE8 in Skellefteå) and 13.0 mm/yr (UME6 in Umeå) provided by Schumacher et al. (2018), (see Fig. 9a). Especially their results of SKE8 and UME6 should be treated with caution, as these were very young stations with short time spans at the time the data were processed for the global database. The difference to SKE0 might be related to the different elastic models and time spans considered, and to a small fraction to different reference frames. Values between 9.2 and 9.8 mm/yr instead are provided by the data-driven GIA models of Simon et al. (2018), (Fig. 9b), which agrees with our GIA model result of about 9.5 mm/yr (Fig. 9c).

Compared to the GIA models, the database of Schumacher et al. (2018) additionally exhibits an unusual GIA uplift pattern in Central Europe. While both GIA models generally show subsidence south of the Baltic Sea (Fig. 9), the global GNSS database shows subsidence in the south-western Netherlands, Belgium and southern England. Also, quite high subsidence of almost 1.9 mm/yr is calculated for Moscow. Such pattern of very high land uplift (more than 11.0 mm/yr) in the Gulf of Bothnia and no subsidence in northern Central Europe and the southern Baltic countries does not agree to current knowledge of the GIA behaviour in Fennoscandia as supported by many observations and modelling studies (see e.g., Steffen and Wu, 2011). Hence, we recommend that this database should be further filtered or re-analysed before
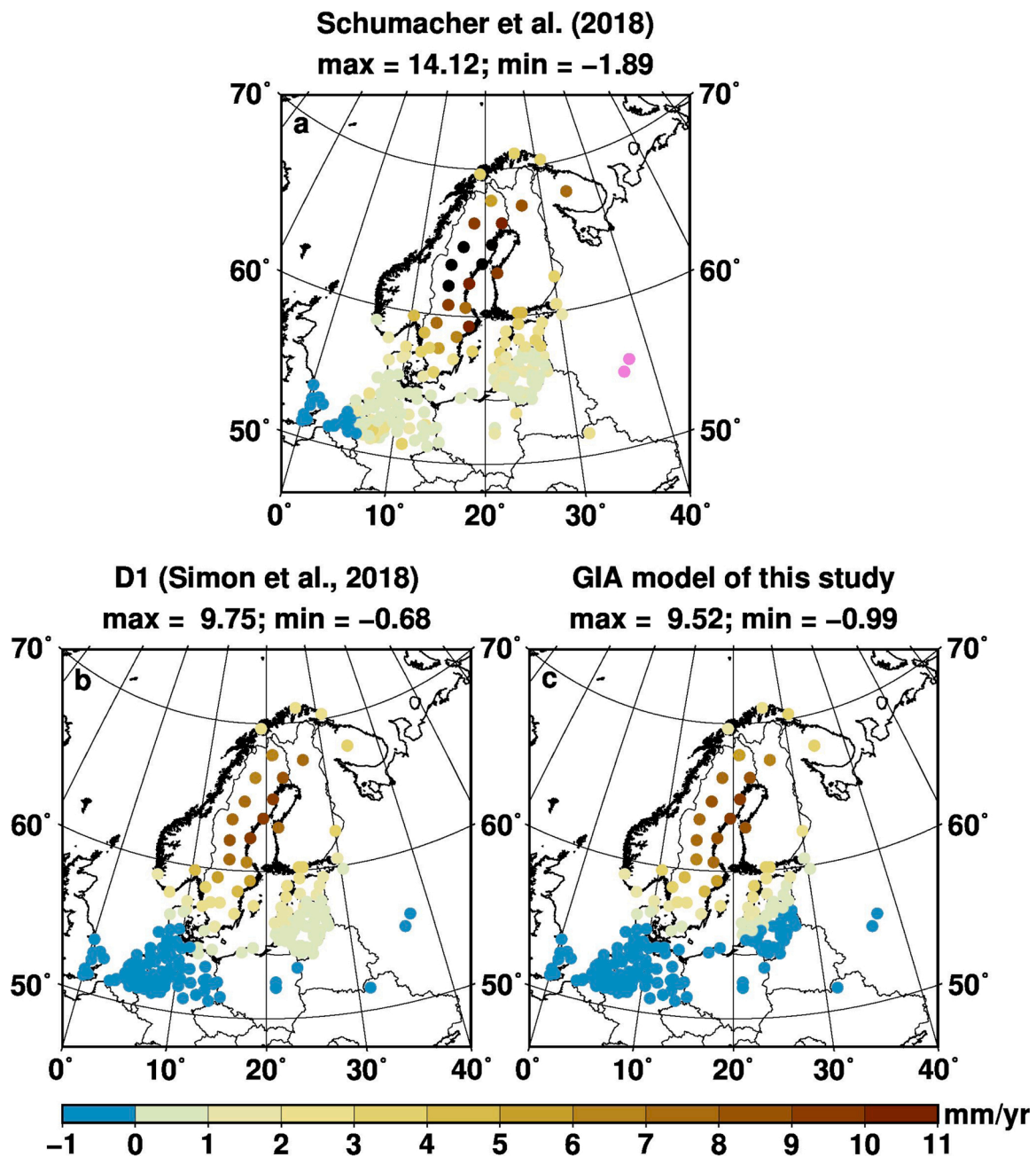
**Fig. 9.** Comparison of vertical velocity in Fennoscandia (a) from the GNSS database of Schumacher et al. (2018), limited to Northern Europe north of 51 degrees, (b) extrapolated from the D1 data-driven GIA model by Simon et al. (2018) at the station coordinates of Schumacher et al. (2018), and (c) same as (b) but for the GIA model used in our study.

being applied in GIA studies for Fennoscandia.

In Fig. 10 we show our transformed velocity field in the GIA frame. The typical uplift pattern remains with slightly reduced maximum values of now ca. 9.3 mm/yr for UME0 and SKE0. The hinge line in the west is moved a bit to the south, while in the east it is at about the same position. The horizontal velocities show the expected GIA pattern of outward motion with maxima of a bit less than 2 mm/yr. Their values in the north and in the south (especially in the forebulge area) are close to zero.

*5.3. A velocity field after elastic and GIA correction – discussion of the residual*

The GIA pattern agrees visually to the one from our selected GIA

model in Fig. 5. This allows analysis of the residual field when the velocity field of the GIA model is removed from the elastically corrected observations. The residual is depicted in Fig. 11. As the observations and elastic models have uncertainties, we have masked all vertical rate residuals within ±0.4 mm/yr and only discuss values larger than this. Using ±0.4 mm/yr also agrees with the mean difference of the GIA model to the elastically corrected observations.

Overall, most differences in the vertical component away from the Atlantic coast are within this ±0.4 mm/yr limit. Residual vertical rates exceeding ±0.4 mm/yr are found along most parts of the Norwegian coast and at the western Baltic Sea coast of Finland. In addition, there are a few isolated spots which may point to station outliers or local deformation, e.g., in eastern Denmark. Differences in the horizontals are generally much less than 1 mm/yr. For many stations, especially in
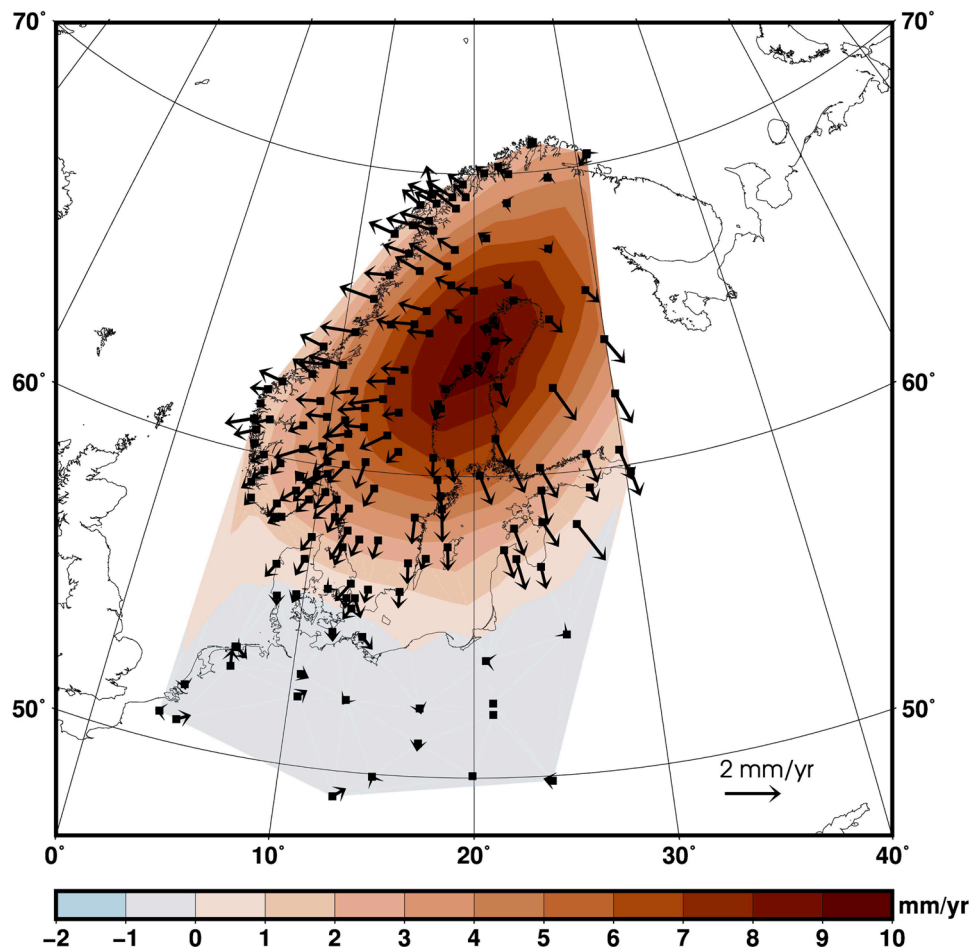
**Fig. 10.** Same as Fig. 8 but in the GIA frame of our GIA model. Note the different scale of the horizontal velocities compared to Fig. 8.

southern Fennoscandia and northern Central Europe, they are negligible.

The differences at the western Finnish coast are mainly attributed to two stations in Finland. Here, it is known that growing trees have affected the measurements at these stations (Lahtinen et al., 2019). This has not been considered in our analysis and thus must be taken care of in a future analysis, as done by Lahtinen et al. (2019).

The strong differences of more than 1 mm/yr in central Western Norway may be referred to several different reasons. The anomaly in the Ranafjord area is likely local/regional neotectonics related to east-west crustal spreading as suggested by Olesen et al. (2013) and Kierulf (2017). Here, Dehls et al. (2002) also observed an irregular subsidence pattern of cax. 1 mm/yr with DInSAR permanent scatterer data. It is thus very likely that our residual field captures this regional process.

Moreover, using InSAR, Rouyet et al. (2018) found a subsidence between 1993–2000 of approximately 6 mm/yr around the Storglomvatn reservoir, not far away from Ranafjord. The water level increased by approximately 120 metres during the 1990s. Such small but still visible subsidence was also found for other reservoirs in the world (e.g., Kaufmann and Amelung, 2000; Wang, 2000), and a small visco-elastic relaxation signal may still be detectable with GNSS from 2000-2014. Nowadays the water level of this hydropower plant water reservoir is allowed to vary with ±60 m. The elastic loading signal decreases with distance to the load. At a distance of 35 km the estimated associated elastic vertical variation is ±0.8 mm (Kierulf, 2017). A similar vertical deformation signal can be expected in the vicinity of other hydropower plant water reservoirs (e.g., Steffen and Kaufmann, 2006). Normally the water level in such water reservoir changes in annual cycles and the effect on the rate is insignificant after a few years

of observations. However, close to the water reservoirs and in periods where the water level is constantly changing over time, for instance when a new reservoir is filled, the elastic loading can have large effects on the velocity field.

Along the Norwegian coastal margin, especially from the south to the Ranafjord area, long-term sedimentary loading effects since the last ice age can alter the velocity field. van der Wal and IJpelaar (2017) analysed different sediment loading scenarios included in GIA models. They found an effect of roughly 0.2 mm/yr in this area for the vertical component. However, as our residual is negative this would increase our residual rather than explaining it.

Another process that could be considered are regional effects of offshore oil and gas extraction that may lead to large-scale subsidence of the surface. However, the majority of fields are at least 50 km away from the coast, and subsidence occurs rather locally (Hatchell et al., 2007; Eiken et al., 2008). Hence, such influence is unlikely.

We do not see eye-catching residuals in the Oslo Graben area which may point to anomalous behaviour there, e.g., a faster uplift than the surrounding. At this point, our results may not help in getting a better understanding of the geodynamic situation there (see e.g., Stratford and Thybo, 2011).

Some part of the anomaly in Northern Norway might be related to a different loading scenario that affects the elastic correction of our northernmost GNSS stations. Using radar altimetry, Rose et al. (2019) found significant sea-level anomalies of up to 7 mm/yr at the northern Norwegian coast (observation time span 01/1996–09/2018), much larger than the global average of ca. 3 mm/yr. This local above-average loading effect cannot be fully resolved in our elastic correction model and thus may change the residuals there.
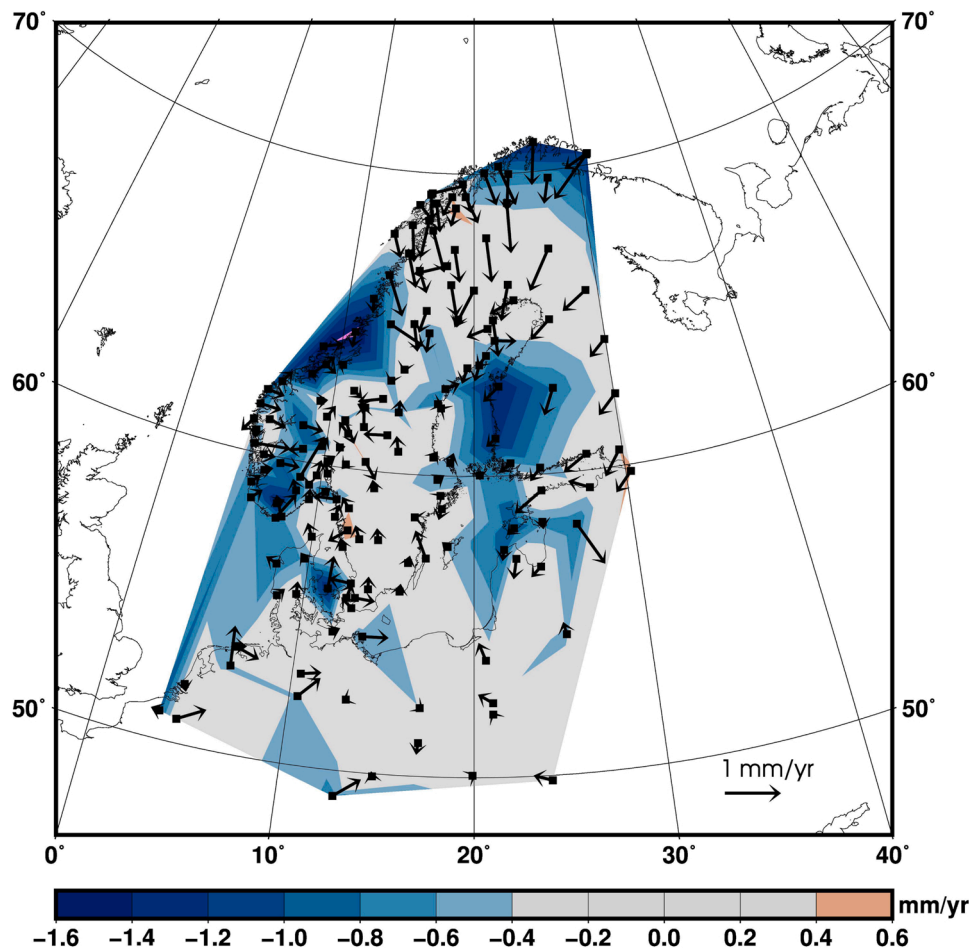
**Fig. 11.** Remaining 3D velocity field in the GIA-frame after removal of the elastic and GIA contributions. Vertical uplift values within ±0.4 mm/yr are not color-coded as they are within observational errors combined with those from the elastic correction models. Contours are drawn with Delauney triangulation of the GMT5 software.

In turn, the residual field may indicate possible improvements in the GIA model. We use a laterally homogeneous Earth model in the GIA model, but the lithosphere should be much thinner along most parts of the Norwegian coast than in central Fennoscandia (e.g., Steffen and Kaufmann, 2005; Fjeldskaar and Bondevik, 2020). Fjeldskaar and Bondevik (2020) even suggest differences in lithospheric thickness between the northern and southern parts of Norway. In addition, Maystrenko et al. (2020) recently pointed to prominent, low-velocity, and, most likely, thermally anomalous zones in the upper mantle of Western and Northern Norway. If these structures are considered in a laterally heterogeneous GIA model, they could alter the velocity field from the GIA model. The latter could be the case in the northern parts, where the horizontal velocity field exhibits differences of up to 1 mm/yr southward. If effects from subsurface structures and tectonics can be excluded, another possibility is the improvement of the ice load history model.

Lastly, we compare our residual field to the one provided by Frederikse et al. (2019), see Fig. 12. We have limited the residual field by Frederikse et al. (2019) to the area of the official Nordic land uplift model NKG2016LU (Vestøl et al., 2019) (49–75 degrees North, 0–50 degrees East). A brief statistical analysis is presented in Fig. 13. The residual field of Frederikse et al. (2019) contains about 210 stations more than our dataset, but these are mainly stations in northern Central Europe and the Baltic countries. The spread in the residual is large (almost 14 mm/yr) with locally very high values of some millimetres per year (Figs. 12b and 13b). Compared to it, our residual field shows only small variation (Figs. 12a and 13a).

If stations with values within ±0.4 mm/yr are removed (Figs. 12e and f), the residual field of Frederikse et al. (2019) shows cluster regions with uplift (Belgium, Czech Republic, south-western Sweden, Gulf of Bothnia and northern Fennoscandia, Moscow) and subsidence (Baltic countries, Denmark). An interpretation of these clusters, e.g., in a geodynamic sense, is difficult. The subsidence in Denmark and the Baltic countries as well as the uplift in northern Fennoscandia may point to improvements in the GIA model used by Frederikse et al. (2019).

We have further limited both datasets to the 60 GNSS stations that are part of each dataset (Figs. 12c and d and 13c and d). With the exception of a few stations in northern Fennoscandia and in Central Europe, the pattern is comparable. Both differences point to possible improvements in the used GIA models. However, we suggest that further filtering of the Frederikse et al. (2019) dataset should be performed to remove some significant outliers in Northern Europe, i.e. those that have residuals exceeding ±2 mm/yr (for comparison, 2 mm/yr is roughly the spread for the 60 stations in our dataset). Such large outliers cannot be confirmed with our dataset nor do we think they are solely related to the GIA model used by Frederikse et al. (2019).

## 6. Conclusions

We provide quality-assessed 3D velocities including uncertainties for 164 GNSS stations in Northern Europe. After ca. 5 years of observation, velocity estimates converge below 0.5 mm/yr RMS and allow a robust analysis. The vertical velocities show a clear uplift signal that relates to glacial isostatic adjustment, while horizontal velocities show north-
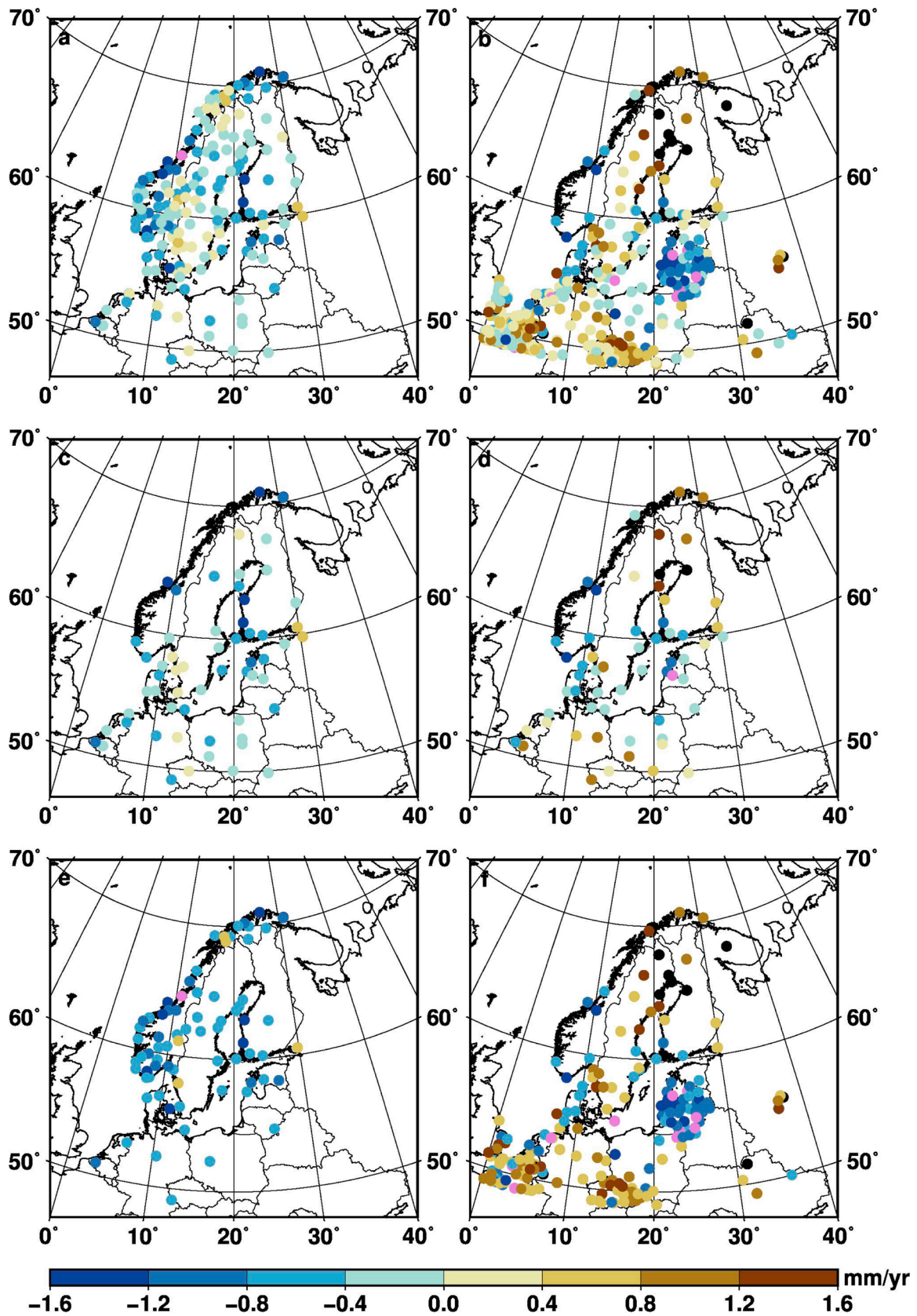
**Fig. 12.** Comparison of residual vertical velocity component of our study (a, c, e) to Frederikse et al. (2019) (b, d, f). (a) and (b) all stations, (c) and (d) only those 60 stations that were used in both studies, (e) and (f) just stations where residuals are smaller than − 0.4 mm/yr or larger than 0.4 mm/yr.
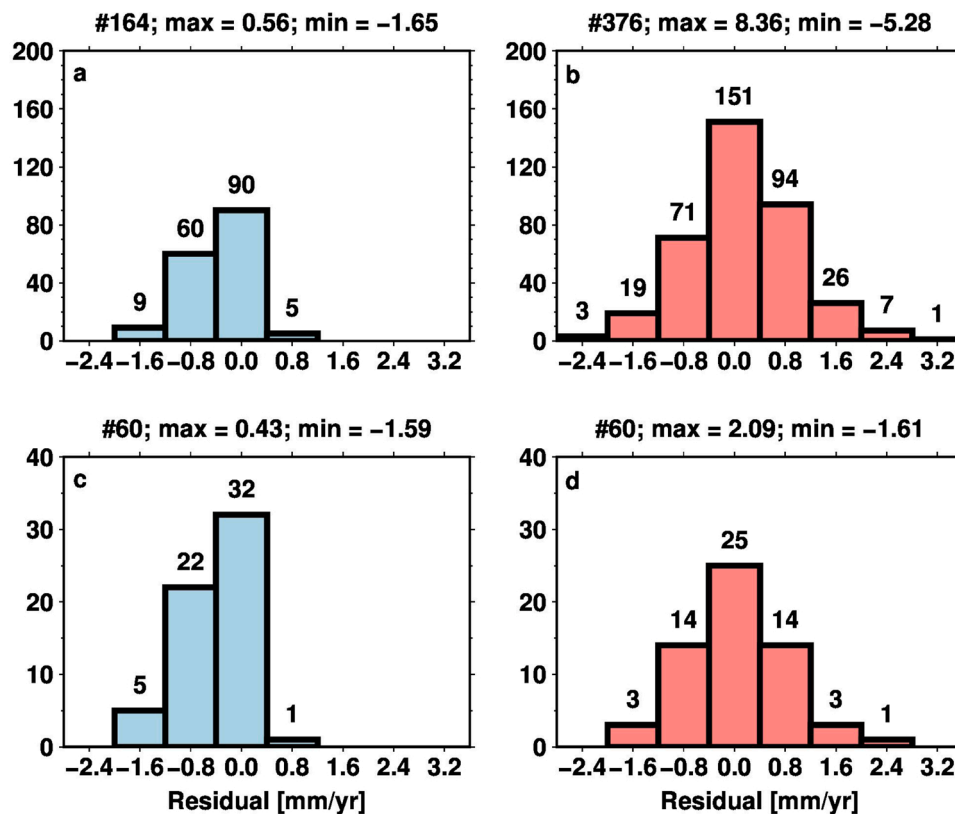
**Fig. 13.** Histograms of the residual vertical velocity component shown in Fig. 12a–d, respectively.

eastward motion of the European plate. When transformed into the reference frame of GIA, the horizontal velocities show a typical pattern of outward motion from the centre of rebound.

Ongoing far field ice melt and regional hydrological changes result in an elastic signal which largely affects the uplift component up to 1 mm/yr, which can be for some stations, e.g., near the hinge line of GIA, larger than the observed velocity. Based on new and sophisticated models, we provide a correction of this elastic signal together with (small) corrections for atmospheric and non-tidal ocean loading. We calculate elastic effects for each station individually depending on the time span of GNSS observation at each station, so that different periods of accelerated or slowed ice melting can be covered. We have shown that this is especially important when the difference in time spans in a dataset is large.

We also list velocities of a selected well-fitting GIA model that can be used to remove the GIA signal from an elastic effects-corrected velocity field. This allows further analysis of the residual velocity signal in view of other geodynamic processes, e.g., tectonics, erosion and sedimentation, and local movements, e.g., due to mining. This could give insight on both the quality of the correction, the accuracy of the models used, and potentially on neglected phenomena with a significant local impact. Our preliminary analysis highlights areas of potential interest such as the central Norwegian coast and northern Fennoscandia, where local environmental or technical/instrumental effects at the GNSS station can be very likely excluded. We suggest that laterally heterogeneous GIA models should be investigated and eventually considered for Northern Europe, e.g. GIA models that address the apparent lateral variation in lithospheric thickness. Also, improved geodynamic models, either regional ones such as for Western Norway or on a continental scale, can provide possible corrections of the velocity field.

We compared our results to other available models and datasets. For some of them we suggest an additional careful quality check as we identified several, large outliers in these models and datasets. We emphasize that a careful quality check seems not yet fully possible with automatized processes that were used in these studies, especially when

data are provided on a global scale. Hence, we advise the user to not apply such datasets blindly.

Finally, we note that even our velocity field still contains known (two stations in Western Finland) and perhaps some unknown outliers. Our residual, especially the vertical component (Figs. 11 and 13a), shows a few stations with values much larger than the estimated error that cannot be explained (yet) with other known processes. These stations need further investigation either on the technical side or regarding local environmental effects. Here, it might be interesting to analyse a GNSS dataset with InSAR measurements and perhaps other ground measurements such as levelling. For example, Gido et al. (2020) determined localized subsidence of up to 6 mm/yr in the northern parts of the city of Gävle, Sweden, with levelling and Persistent Scatterer Interferometry (PSI) technique. Such local deformation rates should then be used to further correct velocities from possibly affected GNSS stations before usage in large-scale geodynamic studies.

### Author statement

**Halfdan Pascal Kierulf:** Conceptualization, Methodology, Software, Formal analysis, Writing – Original Draft, Visualization

**Holger Steffen:** Conceptualization, Methodology, Software, Formal analysis, Writing – Original Draft, Visualization

**Valentina R. Barletta:** Methodology, Software, Data curation, Writing – Original Draft, Writing – Review & Editing

**Martin Lidberg:** Conceptualization, Writing – Original Draft

**Jan Johansson:** Writing – Original Draft

**Oddgeir Kristiansen:** Writing – Original Draft

**Lev Tarasov:** Data curation, Writing – Review & Editing

### Declaration of Competing Interest

The authors report no declarations of interest.

## Appendix A. Two-step reference frame realization

The results in this paper are in IGb08. IGb08 is a Global Navigation Satellite System (GNSS) based realization of ITRF2008 (Altamimi et al., 2011), provided by IGS. It is updated to include changes in the network after the realization of ITRF2008 and takes into account the igs08.atx model of antenna phase center variation and offset, but the datum definition (scale, origo and orientation) agrees with ITRF2008. Later the ITRF2014 was published (Altamimi et al., 2016). According to the transformation between ITRF2008 and ITRF2014 the two reference frames agree at a level of a few 0.1 mm/yr, but differences at individual stations may be considerably larger. These reference frames are considered to be the most accurate and reliable for geodetic studies, but might not be the optimal for specific geodynamic studies (see e.g., Argus, 2007; Argus et al., 2011; Kierulf et al., 2014).

A GAMIT solution is normally transformed to the reference frame using a network of stations either globally or for the region of interest. A regional solution removes most of the so-called CM-signal, which is of importance for velocity estimation especially when there are stations with different time spans included in the network. However, the results in a regional solution depend on the geographical extent of the network and the chosen set of regional reference stations (Legrand et al., 2010). We refer the reader to Legrand et al. (2010) for a detailed analysis of the limitations of regional reference frame realizations. To ensure consistency with the global solution, but exploit the advantages of a regional solution, we used a two-step procedure for reference frame realization.

The first step is a traditional global realization. The daily network was minimally constrained (Altamimi et al., 2002) to IGb08 using 64 globally distributed stations (see Fig. 2). Based on time-series analysis of the daily coordinates for the stations in this global realization, positions and velocities were estimated for all the BIFROST2015 stations. This set of station positions and velocities constitutes the first-step global reference frame.

In the second step, the procedure was repeated, but this time the daily network was minimally constrained to the first-step global reference frame using the vast majority of the BIFROST2015 stations. This two-step procedure (e.g., Lidberg et al., 2009) using the dense-network stabilization is more robust since there is a stronger realization of the frame on each day. This approach removes most of the so-called common mode biases from the daily co-ordinates, but the reference frame retains the connection to the global reference frame.

## Appendix B. Snow disturbance

Snow and ice during winter time can cover GNSS stations in Fennoscandia distorting the estimated station coordinates (e.g., Jaldehag et al., 1996). Large amounts of snow accumulate especially in the more continental climate of the northern parts of Fennoscandia. Stations in Finland (e.g., KEVO, KIVE, KUUS, OULU, ROMU, SODA, and VAAS) and the stations in Kiruna (KIRU and KIR0) in Sweden experience this annually. Also stations like OSLS,
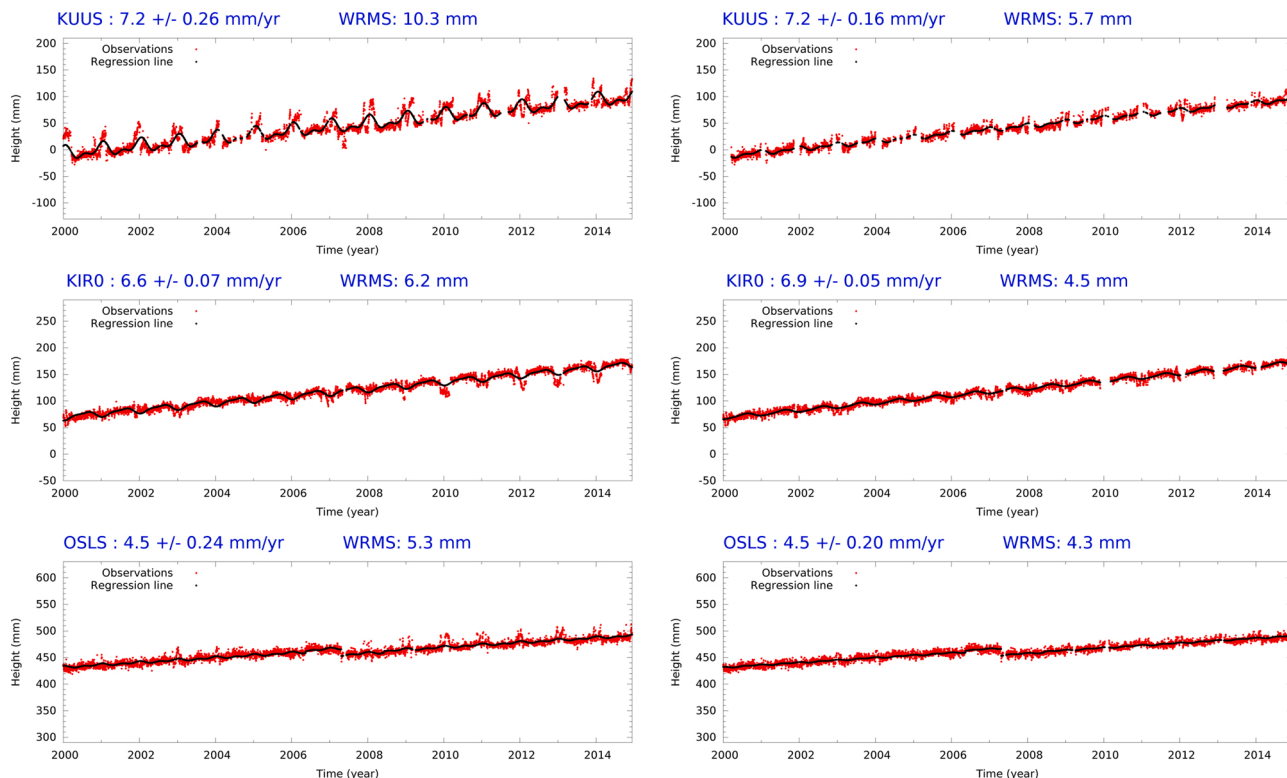


**Fig. B.14.** Examples of improvements in 15 years time-series of the vertical component from three stations affected with snow. Left time-series according to standard analysis, right with an additional iteration, see text for details.

TRYS and TRDS in Norway and ARJ0, LEK0 and VIL0 in Sweden are all clearly influenced (see examples in Fig. B.14). For the stations OSLS and KIR0 we observe increased disturbances after 2006/7. For OSLS the antenna was changed from a choke ring to a zephyr antenna in 2007, at KIR0 there has been a "defroster" test installation using circulating heated air in the radome from about 2004 to 2007. This indicates that changes in the equipment might change the sensitivity to snow.

Such a large amount of outliers in a particular period could distort the computation of both secular rates and harmonic signal and should therefore be removed. Larson (2013) presented a methodology to remove outliers due to snow and ice. The methodology uses the signal strength data to identify the data points affected. As long as the geophysical behaviour of the station is fairly well known it is possible to remove the outliers in the ordinary time-series analysis. However, since the rate and harmonic signals are influenced by the outliers, a normal outlier detection, e.g., at the $3\sigma$ level, does not work satisfactorily. An often used alternative is to manually remove the winter outliers by e.g., the GAMIT module Tsview. We have used another approach by including an additional iteration in the time-series analysis. In this additional iteration, vertical positions from the winter months (October, 20 to April 20) were down-weighted and outliers at the $4.5\sigma$ level relative to this "summer" solution are removed.

We have also assumed that if such gross outliers occur with a few days interval (less than three days), the days between are most likely affected by snow and are thus removed. Even though these intermediate days have small residuals, we assume that they most likely are also influenced by snow and therefore do not belong to the same statistical sample as the other "good" data points. This last assumption does not influence the rate estimate, but might have an impact on the noise characteristic and hence the uncertainty estimation.

Fig. B.14 shows, as an example, time series of the vertical component from three of the snow-exposed stations. The result from the standard time-series analysis is shown in the left column while the result from a time-series analysis including this additional iteration is plotted in the right column. We note a considerable improvement of the WRMS of the time series when the additional iteration is applied. Note that the rate is not affected for KUUS where the outliers are evenly distributed over the whole time series, while for KIR0, which is only affected in the second half of the time series, we see a 0.3 mm/yr shift in the rate.

## Appendix C. Time-series comparison

It is widely recognized that GNSS time series have a more complex noise structure than only white noise (Johnson and Agnew, 1995; Zhang et al., 1997; Mao et al., 1999; Williams, 2003; Williams et al., 2004). This fact has limited consequences on the velocity estimates, but the choice of noise model has significant impact on the estimated uncertainties.

In Table C.1 the RMS and mean deviation of the differences in rate between Cheetah and CATS are included. The differences are negligible. The average estimated uncertainties for the station rates estimated with Cheetah are 5%, 6% and 6% higher in the north, east and vertical component, respectively, than the uncertainties estimated with CATS. CATS includes the daily position uncertainties into the time-series analysis, consequently its daily positions with high uncertainties are down-weighted in the analysis. In Cheetah all points have equal weight and bad points will have more influence on the rates and uncertainty estimates.

The choice of noise model has little effect on the estimated rates. For less than 3% of the stations we find differences in east and west (resp. height) exceeding 0.1 mm/yr (resp. 0.2 mm/yr) between power-law noise, where the spectral index is estimated, and flicker noise, where the spectral index is fixed to $-1$, see Table C.1 for average values.

The estimated mean uncertainties of the rates assuming flicker noise are 10%, 21% and 37% higher in the north, east and vertical component, respectively, than the power law where the spectral index is estimated. The estimated spectral index for the power law solution varies between $-0.3$ and $-1.9$ with a mean of $-0.8$. Most time series have an estimated spectral index higher than $-1$, i.e. most stations are "whiter" than flicker noise. Hence, assuming flicker noise gives in most cases more pessimistic uncertainty estimates.

The time-series analysis indicates no systematic differences between the global solutions from the first step and the solution using the two-step approach. The mean difference are 0.01 mm/yr in the horizontal component and 0.04 mm/yr in the vertical. The RMS of the differences are around 0.05 mm/yr horizontally and slightly below 0.2 mm/yr in the vertical component (see Table C.1).

**Table C.1**
Comparison of horizontal and vertical rate estimates from different solutions of the time-series analysis.

|  | North RMS | East RMS | Up RMS | North MD | East MD | Up MD |
|---|---|---|---|---|---|---|
| CATS[a] | 0.05 | 0.04 | 0.07 | 0.01 | 0.01 | 0.01 |
| WH+FL | 0.04 | 0.04 | 0.08 | 0.00 | 0.00 | 0.02 |
| WH | 0.12 | 0.10 | 0.16 | $-0.02$ | 0.00 | $-0.04$ |
| Global | 0.04 | 0.06 | 0.17 | 0.02 | 0.01 | 0.04 |

The numbers are RMS and mean deviation (MD) between the preferred solution (PS) and other solutions. The PS is the GAMIT solution where the two-step procedure is used in the reference frame realization and the time series are analysed with Cheetah including white noise and power-law noise. The other solutions are: CATS, same as PS except using CATS instead of Cheetah. WH+FL, same as PS except using a fixed power-law index of $-1$ (flicker noise) instead of estimating the power-law index. WH, same as PS except only white noise is assumed present in the time series. Global, same as PS except that we use the global solution from the reference frame realisation omitting the second step described in Appendix A. Units are in mm/yr.

[a] Only a randomly chosen subset of the stations was included in the comparison.

## Appendix D. GIA-frame approach

To avoid problems with plate tectonic and reference frame biases or uncertainties, Kierulf et al. (2014) developed the GIA-frame approach. Each station in the GNSS network has a position in a global reference frame ($\vec{X_i}$). For a given GIA model, we predict velocities for all the stations in the network ($\vec{v_i^{\mathrm{GIA}}}$). These velocities are given relative to some origin, orientation and scale implicitly given by the GIA model. Hence, this list of positions and velocities defines a reference frame consistent with the parameters in the GIA model. This reference frame is named the GIA-reference frame (Kierulf et al., 2014).

Our GNSS velocity field is given by velocity vectors ($\vec{v_i^{\mathrm{GPS}}}$) in a global reference frame (IGb08). This velocity field is transformed, after elastic effects are removed from the vertical component, to the GIA-reference frame with a similarity transformation. The following observation equation is used for the similarity transformation of the velocity field between IGb08 and the GIA-reference frame:

$$\vec{v_i^{\mathrm{GPS}}} = \vec{v_i^{\mathrm{GIA}}} + \begin{pmatrix} s & -\omega_3 & \omega_2 \\ \omega_3 & s & -\omega_1 \\ -\omega_2 & \omega_1 & s \end{pmatrix} \vec{X_i} + \begin{pmatrix} t_1 \\ t_2 \\ t_3 \end{pmatrix} + \vec{r_i^{\mathrm{GPS}}}, \tag{D.1}$$

The unknowns are the three elements of the rotation matrix ($\omega_j, j \in 1,2,3$), the three elements of the translation vector ($t_j, j \in 1,2,3$) and the scale rate parameter ($s$). The residual vector is $\vec{r_i^{\mathrm{GPS}}}$. The observed velocities in the GIA-frame are then $\vec{v_{i,\mathrm{GIA}}^{\mathrm{GPS}}} = \vec{v_i^{\mathrm{GIA}}} + \vec{r_i^{\mathrm{GPS}}}$.

For smaller regional networks the transformation parameters are strongly correlated. For such regional networks it is therefore better to exclude the scale parameters or the translation parameters from the transformation.

## Appendix E. Description of supplement

The table in the supplement contains the final velocity values of the BIFROST2015 network, the elastic corrections during the observation time span of each station and their transformed values into the glacial isostatic adjustment (GIA) frame. Velocities of a well-fitting GIA model are also added. All velocities and RMS in mm/yr. Code = station code, lat = latitude, lon = longitude, yrs = observation time span until 2015.0 [in years], N = horizontal north, E = horizontal east, U = vertical, RMS = uncertainty, SI = spectral index, ais = elastic correction due to ice-mass changes in Antarctica, gis = elastic correction due to ice-mass changes of the Greenland ice sheet, ggl = elastic correction due to ice-mass changes of glaciers in Greenland, gla = elastic correction due to ice-mass changes of global glaciers, tws = elastic correction due to global hydrological changes, sum_h = sum of elastic corrections from global ice-mass changes and hydrology, atm = atmospheric loading changes, nto = non-tidal ocean loading changes, sum_t = total elastic correction, fra = transformed velocity field in the GIA frame, GIA = velocity field of the well-fitting GIA model.

## Appendix A. Supplementary data

Supplementary data associated with this article can be found, in the online version, at https://doi.org/10.1016/j.jog.2021.101845.

## References

Ågren, J., Svensson, R., 2007. Postglacial Land Uplift Model and System Definition for the New Swedish Height System RH 2000.

Altamimi, Z., Collilieux, X., Métivier, L., 2011. ITRF2008: an improved solution of the international terrestrial reference frame. J. Geod. 85, 457–473. https://doi.org/10.1007/s00190-011-0444-4.

Altamimi, Z., Rebischung, P., Métivier, L., Collilieux, X., 2016. ITRF2014: a new release of the international terrestrial reference frame modeling nonlinear station motions. J. Geophys. Res.: Solid Earth 121, 6109–6131. https://doi.org/10.1002/2016JB013098.

Altamimi, Z., Sillard, P., Boucher, C., 2002. A new release of the international terrestrial reference frame for earth science applications. J. Geophys. Res. 107, 2214. https://doi.org/10.1029/2001JB000561.

Argus, D.F., Fu, Y., Landerer, F.W., 2014. Seasonal variation in total water storage in California inferred from GPS observations of vertical land motion. Geophys. Res. Lett. 41, 1971–1980. https://doi.org/10.1002/2014GL059570.

Argus, D.F., Gordon, R.G., DeMets, C., 2011. Geologically current motion of 56 plates relative to the no-net-rotation reference frame. Geochem. Geophys. Geosyst. https://doi.org/10.1029/2011GC003751.

Argus, F.A., 2007. Defining the translation velocity of the reference frame of earth. Geophys. J. Int. 169, 830–838. https://doi.org/10.1111/j.1365-246X.2007.03344.x.

Artemieva, I.M., 2019. Lithosphere structure in Europe from thermal isostasy. Earth-Sci. Rev. 188, 454–468. https://doi.org/10.1016/j.earscirev.2018.11.004.

Bergstrand, S., Scherneck, H.G., Milne, G.A., Johansson, J.M., 2005. Upper mantle viscosity from continuous GPS baselines in Fennoscandia. J. Geodyn. 39, 91–109. https://doi.org/10.1016/j.jog.2004.08.004.

Bilker-Koivula, M., Mäkinen, J., Ruotsalainen, H., Näränen, J., Saari, T., 2021. Forty-three years of absolute gravity observations of the Fennoscandian postglacial rebound in Finland. J. Geod. 95 https://doi.org/10.1007/s00190-020-01470-9.

Blewitt, G., Hammond, W., Kreemer, C., 2018. Harnessing the GPS data explosion for interdisciplinary science. Eos 99. https://doi.org/10.1029/2018EO104623.

Boehm, J., Werl, B., Schuh, H., 2006. Troposphere mapping functions for GPS and very long baseline interferometry from European centre for medium-range weather forecasts operational analysis data. J. Geophys. Res. 111, B02406. https://doi.org/10.1029/2005JB003629.

Bogusz, J., Klos, A., Pokonieczny, K., 2019. Optimal strategy of a GPS position time series analysis for post-glacial rebound investigation in Europe. Remote Sens. 11 https://doi.org/10.3390/rs11101209.

Bos, M., Fernandes, R., Williams, S., Bastos, L., 2008. Fast error analysis of continuous GPS observations. J. Geod. 82, 157–166. https://doi.org/10.1007/s00190-007-0165-x.

Cáceres, D., Marzeion, B., Malles, J.H., Gutknecht, B.D., Müller Schmied, H., Döll, P., 2020. Assessing global water mass transfers from continents to oceans over the period 1948–2016. Hydrol. Earth Syst. Sci. 24, 4831–4851. https://doi.org/10.5194/hess-24-4831-2020.

Compton, K., Bennett, R.A., Hreinsdóttir, S., van Dam, T., Bordoni, A., Barletta, V., Spada, G., 2017. Short-term variations of Icelandic ice cap mass inferred from cGPS coordinate time series. Geochem. Geophys. Geosyst. 18, 2099–2119. https://doi.org/10.1002/2017GC006831.

Dehls, J.F., Basilico, M., Colesanti, C., 2002. Ground deformation monitoring in the Ranafjord area of Norway by means of the permanent scatterers technique. IEEE International Geoscience and Remote Sensing Symposium, vol. 1 203–207. https://doi.org/10.1109/IGARSS.2002.1024988.

Dobslaw, H., Thomas, M., 2007. Simulation and observation of global ocean mass anomalies. J. Geophys. Res.: Oceans 112. https://doi.org/10.1029/2006JC004035.

Döll, P., Kaspar, F., Lehner, B., 2003. A global hydrological model for deriving water availability indicators: model tuning and validation. J. Hydrol. 270, 105–134. https://doi.org/10.1016/S0022-1694(02)00283-4.

Eiken, O., Stenvold, T., Zumberge, M., Alnes, H., Sasagawa, G., 2008. Gravimetric monitoring of gas production from the Troll field. Geophysics 73, WA149–WA154. https://doi.org/10.1190/1.2978166.

Ekman, M., 2009. The Changing Level of the Baltic Sea During 300 Years: A Clue to Understanding the Earth.

Farrell, W.E., Clark, J.A., 1976. On postglacial sea level. Geophys. J. R. Astron. Soc. 46, 647–667. https://doi.org/10.1111/j.1365-246X.1976.tb01252.x.

FENCAT, 2020. Fennoscandian Earthquake Catalogue for 1375–2014. http://www.seismo.helsinki.fi/bulletin/list/catalog/FENCAT.html.

Fjeldskaar, W., Bondevik, S., 2020. The Early-Mid Holocene transgression (Tapes) at the Norwegian coast – comparing observations with numerical modelling. Quat. Sci. Rev. 242, 106435. https://doi.org/10.1016/j.quascirev.2020.106435.

Frederikse, T., Landerer, F.W., Caron, L., 2019. The imprints of contemporary mass redistribution on local sea level and vertical land motion observations. Solid Earth 10, 1971–1987. https://doi.org/10.5194/se-10-1971-2019.

Frederikse, T., Riva, R., Kleinherenbrink, M., Wada, Y., van den Broeke, M., Marzeion, B., 2016. Closing the sea level budget on a regional scale: trends and variability on the Northwestern European continental shelf. Geophys. Res. Lett. 43, 10864–10872. https://doi.org/10.1002/2016GL070750.

Gido, N.A.A., Bagherbandi, M., Nilfouroushan, F., 2020. Localized subsidence zones in Gävle City detected by sentinel-1 PSI and leveling data. Remote Sens. 12 https://doi.org/10.3390/rs12162629.

Gradmann, S., Olesen, O., Keiding, M., Maystrenko, Y., 2018. The regional 3D stress field of Nordland, northern Norway – insights from numerical modelling. In: Olesen, O., Janutyte, I., Michálek, J., Keiding, M., Lindholm, C., Kierulf, H.P., Ottemöller, L., Gradmann, S., Maystrenko, Y.P., Rouyet, L., Lauknes, T.R., Dehls, J.F., Ask, M., Ask, D., Olsen, L., Ottesen, D., Rise, L., Riis, F., Drottning, A., Tjåland, A., Strømme, M., Storheim, B., Rodenay, S. (Eds.), Neotectonics in Nordland – Implications for Petroleum Exploration (NEONOR2), pp. 215–240.

Gregersen, S., Lindholm, C., Korja, A., Lund, B., Uski, M., Oinonen, K., Voss, P.H., Keiding, M., 2021. Seismicity and sources of stress in Fennoscandia. In: Steffen, H., Olesen, O., Sutinen, R. (Eds.), Glacially-Triggered Faulting. Cambridge University Press, Cambridge, pp. 160–179. https://doi.org/10.1017/9781108779906. In press.

Gregersen, S., Voss, P., TOR Working Group, 2002. Summary of project TOR: delineation of a stepwise, sharp, deep lithosphere transition across Germany-Denmark-Sweden. Tectonophysics 360, 61–73. https://doi.org/10.1016/S0040-1951(02)00347-5.

Häkli, P., Lidberg, M., Jivall, L., Steffen, H., Kierulf, H.P., Ågren, J., Vestøl, O., Lahtinen, S., Steffen, R., Tarasov, L., 2019. New horizontal intraplate velocity model for Nordic and Baltic countries. In: Proceedings of the 81th FIG Working Week "Geospatial information for a smarter life and environmental resilience". FIG, pp. 1–15. In: http://www.fig.net/resources/proceedings/fig_proceedings/fig2019/papers/ts01e/TS01E_haekli_lidberg_et_al_10078.pdf.

Hatchell, P.J., Jorgensen, O., Gommesen, L., Stammeijer, J., 2007. Monitoring reservoir compaction from subsidence and time-lapse time shifts in the Dan field. SEG Technical Program Expanded Abstracts 2007 2867–2871. https://doi.org/10.1190/1.2793062.

Herring, T., King, R., Floyd, M., McClusky, S., 2015. Introduction to GAMIT/GLOBK Release 10.6. Mass. Instit. of Technol., Cambridge. Technical Report.

Hill, E.M., Davis, J.L., Tamisiea, M.E., Lidberg, M., 2010. Combination of geodetic observations and models for glacial isostatic adjustment fields in Fennoscandia. J. Geophys. Res. 115 https://doi.org/10.1029/2009JB006967.

Horwath, M., Novotny, K., Cazenave, A., Palanisamy, H.K., Marzeion, B., Paul, F., Doell, P., Caceres, D., Hogg, A.E., Otosaka, I., Shepherd, A., Forsberg, R., Barletta, V. R., Andersen, O.B., Rose, S.K., Johannessen, J.A., Raj, R.P., Gutknecht, B.D., Merchant, C.J., Macintosh, C.R., von Schuckmann, K., 2020. ESA Climate Change Initiative (CCI) Sea Level Budget Closure (SLBC_cci). Final Report (D4.7). Version 1.1.

Hughes, A.L.C., Gyllencreutz, R., Lohne, Ø.S., Mangerud, J., Svendsen, J.I., 2016. The last Eurasian ice sheets – a chronological database and time-slice reconstruction. DATED-1. Boreas 45, 1–45. https://doi.org/10.1111/bor.12142.

Jaldehag, R.T.K., Johansson, J.M., Davis, J.L., Elósegui, P., 1996. Geodesy using the swedish permanent gps network: effects of snow accumulation on estimates of site positions. Geophys. Res. Lett. 23, 1601–1604. https://doi.org/10.1029/96GL00970.

Johansson, J., Davis, J., Scherneck, H.G., Milne, G., Vermeer, M., Mitrovica, J., Bennett, R., Jonsson, B., Elgered, G., Elosegui, P., Koivula, H., Poutanen, M., Ronnang, B., Shapiro, I., 2002. Continous GPS measurements of postglacial adjustment in Fennoscandia 1. Geodetic result. J. Geophys. Res. 107, 2157. https://doi.org/10.1029/2001 JB000400.

Johnson, H.O., Agnew, D.C., 1995. Monument motion and measurements of crustal velocities. Geophys. Res. Lett. 22 (21), 2905–2908. https://doi.org/10.1029/95GL02661.

Kaufmann, G., 2000. Ice-ocean mass balance during the Late Pleistocene glacial cycles in view of CHAMP and GRACE satellite missions. Geophys. J. Int. 143, 142–156. https://doi.org/10.1046/j.1365-246x.2000.00223.x.

Kaufmann, G., 2004. Program Package ICEAGE, Version 2004. Manuscript. Institut für Geophysik der Universität Göttingen.

Kaufmann, G., Amelung, F., 2000. Reservoir-induced deformation and continental rheology in vicinity of Lake Mead, Nevada. J. Geophys. Res.: Solid Earth 105, 16341–16358. https://doi.org/10.1029/2000JB900079.

Kaufmann, G., Lambeck, K., 1997. Implications of late pleistocene glaciation of the Tibetan Plateau for present-day uplift rates and gravity anomalies. Quat. Res. 48, 267–279. https://doi.org/10.1006/qres.1997.1924.

Kaufmann, G., Lambeck, K., 2000. Mantle dynamics, postglacial rebound and the radial viscosity profile. Phys. Earth Planet. Inter. 121, 301–324. https://doi.org/10.1016/S0031-9201(00)00174-6.

Kaufmann, G., Lambeck, K., 2002. Glacial isostatic adjustment and the radial viscosity profile from inverse modeling. J. Geophys. Res.: Solid Earth 107. https://doi.org/10.1029/2001JB000941. ETG 5-1-ETG 5-15.

Keiding, M., Kreemer, C., Lindholm, C.D., Gradmann, S., Olesen, O., Kierulf, H.P., 2015. A comparison of strain rates and seismicity for Fennoscandia: depth dependency of deformation from glacial isostatic adjustment. Geophys. J. Int. 202, 1021–1028. https://doi.org/10.1093/gji/ggv207.

Kierulf, H.P., 2017. Analysis strategies for combining continuous and episodic GNSS for studies of neo-tectonics in Northern-Norway. J. Geodyn. 109, 32–40. https://doi.org/10.1016/j.jog.2017.07.002.

Kierulf, H.P., Ouassou, M., Simpson, M., Vestøl, O., 2013. A continuous velocity field for Norway. J. Geod. 87, 337–349. https://doi.org/10.1007/s00190-012-0603-2.

Kierulf, H.P., Plag, H.P., Kristiansen, O., 2003. Towards the true rotation of a rigid eurasia. In: Torres, J.A., Hornik, H. (Eds.), EUREF Publication No. 12, Verlag des Bundesamtes für Kartographie und Geodäsie. Frankfurt am Main, pp. 118–124.

Kierulf, H.P., Steffen, H., Simpson, M.J.R., Lidberg, M., Wu, P., H.,W, 2014. A GPS velocity field for Fennoscandia and a consistent comparison to glacial isostatic adjustment models. J. Geophys. Res.: Solid Earth 119, 6613–6629. https://doi.org/10.1002/2013JB010889.

King, R.W., Bock, Y., 2003. Documentation for the GAMIT Analysis Software, Release 10.1. Massachusetts Institute of Technology (MIT), Cambridge. Technical Report.

Kollo, K., Spada, G., Vermeer, M., 2016. Studying earth rheology using GNSS permanent stations and GIA modelling tools. Geophysica 51, 3–15. https://doi.org/10.1111/j.1365-246X.2012.05454.x.

Lagerbäck, R., Sundh, M., 2008. Early Holocene Faulting and Paleoseismicity in Northern Sweden. SGU. Geological Survey of Sweden Research Paper, C 836.

Lahtinen, S., Jivall, L., Häkli, P., Kall, T., Kollo, K., Kosenko, K., Galinauskas, K., Prizginiene, D., Tangen, O., Weber, M., Nordman, M., 2019. Densification of the ITRF2014 position and velocity solution in the Nordic and Baltic countries. GPS Solut. 23, 95. https://doi.org/10.1007/s10291-019-0886-3.

Lambeck, K., Smither, C., Johnston, P., 1998. Sea-level change, glacial rebound and mantle viscosity for northern Europe. Geophys. J. Int. 134, 102–144. https://doi.org/10.1046/j.1365-246x.1998.00541.x.

Larson, K.M., 2013. A methodology to eliminate snow- and ice-contaminated solutions from gps coordinate time series. J. Geophys. Res.: Solid Earth 118, 4503–4510. https://doi.org/10.1002/jgrb.50307.

Legrand, J., Bergeot, N., Bruyninx, C., Wöppelmann, G., Bouin, M.N., Altamimi, Z., 2010. Impact of regional reference frame definition on geodynamic interpretations. J. Geodyn. 49, 116–122. https://doi.org/10.1016/j.jog.2009.10.002. WEGENER 2008 – Proceedings of the 14th General Assembly of Wegener.

Lidberg, M., Johansson, J., Scherneck, H., Milne, G., Davis, J., 2009. New results based on reprocessing of 13 years continuous GPS observations of the Fennoscandia GIA process from BIFROST. In: Sideris, M. (Ed.), Observing our Changing Earth. International Association of Geodesy Symposia. Springer, Berlin, Heidelberg, pp. 557–568.

Lidberg, M., Johansson, J., Scherneck, H.G., Davis, J., 2007. An improved and extended GPS derived velocity field for the glacial isostatic adjustment in Fennoscandia. J. Geod. 81, 213–230. https://doi.org/10.1007/s00190-006-0102-4.

Lidberg, M., Johansson, J.M., Scherneck, H.G., Milne, G.A., 2010. Recent results based on continuous GPS observations of the GIA process in fennoscandia from BIFROST. J. Geodyn. https://doi.org/10.1016/j.jog.2009.11.010.

Lindblom, E., Lund, B., Tryggvason, A., Uski, M., Bödvarsson, R., Juhlin, C., Roberts, R., 2015. Microearthquakes illuminate the deep structure of the endglacial Pärvie fault, northern Sweden. Geophys. J. Int. 201, 1704–1716. https://doi.org/10.1093/gji/ggv112.

Ludwigsen, C.A., Khan, S.A., Andersen, O.B., Marzeion, B., 2020. Vertical land motion from present-day deglaciation in the wider Arctic. Geophys. Res. Lett. 47 https://doi.org/10.1029/2020GL088144 e2020GL088144.

Lyard, F., Lefevre, F., Letellier, T., 2006. Modelling the global ocean tides: modern insights from FES2004. Ocean Dyn. 56 https://doi.org/10.1007/s10236-006-0086-x.

Mantovani, M., Scherneck, H.G., 2013. DInSAR investigation in the Pärvie end-glacial fault region, Lapland, Sweden. Int. J. Remote Sens. 34, 8491–8502. https://doi.org/10.1080/01431161.2013.843871.

Mao, A., Harrison, C.G.A., Dixon, T.H., 1999. Noise in GPS coordinate time series. J. Geophys. Res. 104, 2797–2816. https://doi.org/10.1029/1998JB900033.

Martinec, Z., Klemann, V., van der Wal, W., Riva, R.E.M., Spada, G., Sun, Y., Melini, D., Kachuck, S.B., Barletta, V., Simon, K., A.,G, James, T.S., 2018. A benchmark study of numerical implementations of the sea level equation in GIA modelling. Geophys. J. Int. 215, 389–414. https://doi.org/10.1093/gji/ggy280.

Maussion, F., Butenko, A., Champollion, N., Dusch, M., Eis, J., Fourteau, K., Gregor, P., Jarosch, A.H., Landmann, J., Oesterle, F., Recinos, B., Rothenpieler, T., Vlug, A., Wild, C.T., Marzeion, B., 2019. The Open Global Glacier Model (OGGM) v1.1. Geosci. Model Dev. 12, 909–931. https://doi.org/10.5194/gmd-12-909-2019.

Maystrenko, Y.P., Brönner, M., Olesen, O., Saloranta, T.M., Slagstad, T., 2020. Atmospheric precipitation and anomalous upper mantle in relation to intraplate seismicity in Norway. Tectonics 39. https://doi.org/10.1029/2020TC006070 e2020TC006070.

Mazur, S., Mikolajczak, M., Krzywiec, P., Malinowski, M., Buffenmyer, V., Lewandowski, M., 2015. Is the Teisseyre-Tornquist zone an ancient plate boundary of Baltica? Tectonics 34, 2465–2477. https://doi.org/10.1002/2015TC003934.

Milne, G., Davis, J., Mitrovica, J., Scherneck, H.G., Johansson, J., Vermeer, M., Koivula, H., 2001. Space-Geodetic constraints on glacial isostatic adjustments in Fennoscandia. Science 291, 2381–2385. https://doi.org/10.1126/science.1057022.

Milne, G.A., Mitrovica, J.X., Scherneck, H.G., Davis, J.L., Johansson, J.M., 2004. Continuous GPS measurements of postglacial adjustment in Fennoscandia: 2. modeling results. J. Geophys. Res. 109 https://doi.org/10.1029/2003JB002619.

Müller, J., Naeimi, M., Gitlein, O., Timmen, L., Denker, H., 2012. A land uplift model in Fennoscandia combining GRACE and absolute gravimetry data. Phys. Chem. Earth 53, 54–60. https://doi.org/10.1016/J.PCE.2010.12.006.

Müller Schmied, H., Adam, L., Eisner, S., Fink, G., Flörke, M., Kim, H., Oki, T., Portmann, F.T., Reinecke, R., Riedel, C., Song, Q., Zhang, J., Döll, P., 2016. Variations of global and continental water balance components as impacted by climate forcing uncertainty and human water use. Hydrol. Earth Syst. Sci. 20, 2877–2898. https://doi.org/10.5194/hess-20-2877-2016.

Munier, R., Adams, J., Brandes, C., Brooks, G., Dehls, J., Gibbons, S.J., Hjartardóttir, Á. R., Hogaas, F., Johansen, T.A., Kværna, T., Mattila, J., Mikko, H., Müller, K., Nikolaeva, S.B., Ojala, A., Olesen, O., Olsen, L., Palmu, J.P., Ruskeeniemi, T.,

Ruud, B.O., Sandersen, P.B.E., Shvarev, S.V., Smith, C.A., Steffen, H., Steffen, R., Sutinen, R., Tassis, G., 2020. International Database of Glacially Induced Faults. PANGAEA. https://doi.org/10.1594/PANAGAEA.922705.

Nordman, M., Milne, G., Tarasov, L., 2015. Reappraisal of the Ångerman River decay time estimate and its application to determine uncertainty in Earth viscosity structure. Geophys. J. Int. 201, 811–822. https://doi.org/10.1093/gji/gjv051.

Nyberg, S., Kallio, U., Koivula, H., 2013. GPS monitoring of bedrock stability at Olkiluoto nuclear waste disposal site in Finland from 1996 to 2012. J. Geod. Sci. 3, 121–126. https://doi.org/10.2478/jogs-2013-0017.

Ojala, A.E., Markovaara-Koivisto, M., Middleton, M., Ruskeeniemi, T., Mattila, J., Sutinen, R., 2018. Dating of paleolandslides in western Finnish Lapland. Earth Surf. Process. Landf. 43, 2449–2462. https://doi.org/10.1002/esp.4408.

Olesen, O., Kierulf, H.P., Brönner, M., Dalsegg, E., Fredin, O., Solbakk, T., 2013. Deep weathering, neotectonics and strandflat formation in Nordland, northern Norway. Nor. J. Geol. 93, 189–213. Issn:029-196X.

Olesen, O., Olsen, L., Gibbons, S.J., Ruud, B.O., Høgaas, F., Johansen, T.A., Kværna, T., 2021a. Postglacial faulting in Norway: Large magnitude earthquakes of the Late Holocene age. In: Steffen, H., Olesen, O., Sutinen, R. (Eds.), Glacially-Triggered Faulting. Cambridge University Press, Cambridge, pp. 180–197.

Olesen, O., Steffen, H., Sutinen, R., 2021b. Outlook: Future research on glacially triggered faulting and intraplate seismicity. Glacially-Triggered Faulting. Cambridge University Press, Cambridge, pp. 379–387.

Olsson, P.A., Breili, K., Ophaug, V., Steffen, H., Bilker-Koivula, M., Nielsen, E., Oja, T., Timmen, L., 2019. Postglacial gravity change in Fennoscandia – three decades of repeated absolute gravity observations. Geophys. J. Int. 217, 1141–1156. https://doi.org/10.1093/gji/ggz054.

Peltier, W.R., 1974. The impulse response of a Maxwell Earth. Rev. Geophys. 12, 649–669. https://doi.org/10.1029/RG012i004p00649.

Petrov, L., Boy, J.P., 2004. Study of the atmospheric pressure loading signal in VLBI observations. J. Geophys. Res. 109 https://doi.org/10.1029/2003JB002500.

Robin, C.M.I., Craymer, M., Ferland, R., James, T.S., Lapelle, E., Piraszewski, M., Zhao, Y., 2020. NAD83v70VG: A New National Crustal Velocity Model for Canada. https://doi.org/10.4095/327592.

Root, B.C., Tarasov, L., van der Wal, W., 2015. GRACE gravity observations constrain Weichselian ice thickness in the Barents Sea. Geophys. Res. Lett. 42, 3313–3320. https://doi.org/10.1002/2015GL063769.

Rose, S.K., Andersen, O.B., Passaro, M., Ludwigsen, C.A., Schwatke, C., 2019. Arctic Ocean sea level record from the complete radar altimetry era: 1991–2018. Remote Sens. 11 https://doi.org/10.3390/rs11141672.

Rouyet, L., Lauknes, T.R., Larsen, Y., 2018. InSAR deformation analysis for Helgeland. In: Olesen, O., Janutyte, I., Michálek, J., Keiding, M., Lindholm, C., Kierulf, H.P., Ottemöller, L., Gradmann, S., Maystrenko, Y.P., Rouyet, L., Lauknes, T.R., Dehls, J. F., Ask, M., Ask, D., Olsen, L., Ottesen, D., Rise, L., Riis, F., Drottning, A., land, A.T., Strømme, M., Storheim, B., Rodenay, S. (Eds.), Neotectonics in Nordland – Implications for Petroleum Exploration (NEONOR2), pp. 160–179.

Samrat, N.H., King, M.A., Watson, C., Hooper, A., Chen, X., Barletta, V.R., Bordoni, A., 2020. Reduced ice mass loss and three-dimensional viscoelastic deformation in northern Antarctic Peninsula inferred from GPS. Geophys. J. Int. 222, 1013–1022. https://doi.org/10.1093/gji/ggaa229.

Santamaría-Gómez, A., Watson, C., Gravelle, M., King, M.A., Wöppelmann, G., 2014. Levelling co-located GNSS and tide gauge stations using GNSS reflectometry. J. Geod. 89, 241–258. https://doi.org/10.1007/s00190-014-0784-y.

Scherneck, H.G., 1991. A parametrized solid earth tide model and ocean tide loading effects for global geodetic baseline measurements. Geophys. J. Int. 106, 677–694. https://doi.org/10.1111/j.1365-246X.1991.tb06339.x.

Scherneck, H.G., Johansson, J., Elgered, G., Davis, J., Jonsson, B., Hedling, G., Koivula, M., Ollikainen, M., Poutanen, M., Vermeer, M., Mitrovica, J., Milne, G.A., 2002. BIFROST: observing the three-dimensional deformation of Fennoscandia. In: Mitrovica, X., Vermeersen, B.L.A. (Eds.), Ice Sheets Sea Level and the Dynamic Earth. American Geophysical Union, Washington, D.C, pp. 69–93.

Schmidt, P., Lund, B., Näslund, J.O., Fastook, J., 2014. Comparing a thermo-mechanical Weichselian Ice Sheet reconstruction to reconstructions based on the sea level equation: aspects of ice configurations and glacial isostatic adjustment. Solid Earth 5, 371–388. https://doi.org/10.5194/se-5-371-2014.

Schumacher, M., King, M.A., Rougier, J., Sha, Z., Khan, S.A., Bamber, J.L., 2018. A new global GPS data set for testing and improving modelled GIA uplift rates. Geophys. J. Int. 214, 2164–2176. https://doi.org/10.1093/gji/ggy235.

Sella, G.F., Stein, S., Dixon, T.H., Craymer, M., James, T.S., Mazzotti, S., Dokka, R.K., 2007. Observation of glacial isostatic adjustment in "stable" North America with GPS. Geophys. Res. Lett. 34 https://doi.org/10.1029/2006GL027081.

Sigmond, E., 2002. Geological Map, Land and Sea Areas of Northern Europe, Scale 1: 4,000,000.

Simon, K.M., James, T.S., Henton, J.A., Dyke, A.S., 2016. A glacial isostatic adjustment model for the central and northern Laurentide Ice Sheet based on relative sea level and GPS measurements. Geophys. J. Int. 205, 1618–1636. https://doi.org/10.1093/gji/ggw103.

Simon, K.M., Riva, R.E.M., Kleinherenbrink, M., Frederikse, T., 2018. The glacial isostatic adjustment signal at present day in northern Europe and the British Isles

estimated from geodetic observations and geophysical models. Solid Earth 9, 777–795. https://doi.org/10.5194/se-9-777-2018.

Simonsen, S.B., Barletta, V.R., Colgan, W., Sørensen, L.S., 2021. Greenland Ice Sheet mass balance (1992–2020) from calibrated radar altimetry. Geophys. Res. Lett. https://doi.org/10.1029/2020GL091216 n/a, e2020GL091216.

Sjöberg, L.E., Pan, M., Asenjo, E., 2004. Oskarshamn site investigation – A deformation analysis of the äspö GPS monitoring network from 2000 to 2004. Svensk Kärnbränslehantering 63. AB P-04-196.

Steffen, H., Kaufmann, G., 2005. Glacial isostatic adjustment of Scandinavia and northwestern Europe and the radial viscosity structure of the Earth's mantle. Geophys. J. Int. 163, 801–812. https://doi.org/10.1111/j.1365-246X.2005.02740.x.

Steffen, H., Kaufmann, G., 2006. Numerical modelling of deformation changes induced by lake-level fluctuations of the Hohenwarte reservoir, Thuringia, Germany. J. Geodyn. 41, 411–421. https://doi.org/10.1016/j.jog.2005.10.004.

Steffen, H., Olesen, O., Sutinen, R., 2021. Glacially triggered faulting: a historical overview and recent developments. In: Steffen, H., Olesen, O., Sutinen, R. (Eds.), Glacially-Triggered Faulting. Cambridge University Press, Cambridge, pp. 1–17. https://doi.org/10.1017/9781108779906. In press.

Steffen, H., Wu, P., 2011. Glacial isostatic adjustment in Fennoscandia – a review of data and modeling. J. Geodyn. 52, 160–2004. https://doi.org/10.1016/j.jog.2011.03.002.

Steffen, H., Wu, P., Wang, H., 2010. Determination of the Earth's structure in Fennoscandia from GRACE and implications for the optimal post-processing of GRACE data. Geophys. J. Int. 182, 1295–1310. https://doi.org/10.1111/j.1365-246X.2010.04718.x.

Stratford, W., Thybo, H., 2011. Crustal structure and composition of the Oslo Graben, Norway. Earth Planet. Sci. Lett. 304, 431–442. https://doi.org/10.1016/j.epsl.2011.02.021.

Tarasov, L., 2013. GLAC-1b: a new data-constrained global deglacial Ice Sheet reconstruction from glaciological modelling and the challenge of missing ice. In: European Geophysical Union General Assembly 2013. Vienna, Austria, Abstracts, 15, EGU2013-12347.

Tarasov, L., Dyke, A.S., Neal, R.M., Peltier, W., 2012. A data-calibrated distribution of deglacial chronologies for the North American ice complex from glaciological modeling. Earth Planet. Sci. Lett. 315–316, 30–40. https://doi.org/10.1016/j.epsl.2011.09.010 sea Level and Ice Sheet Evolution: A PALSEA Special Edition.

Torsvik, T., Carlos, D., Mosar, J., Cocks, L., Malme, T., 2002. Global reconstructions and North Atlantic palaeogeography 400 Ma to recent. In: Eide, A. (Ed.), BATLAS – Mid Norway Plate Reconstructions Atlas With Global and Atlantic Perspectives. Geological Survey of Norway, pp. 18–39.

Vestøl, O., Ågren, J., Steffen, H., Kierulf, H., Tarasov, L., 2019. NKG2016LU: a new land uplift model for Fennoscandia and the Baltic region. J. Geod. 93, 1759–1779. https://doi.org/10.1007/s00190-019-01280-8.

van der Wal, W., IJpelaar, T., 2017. The effect of sediment loading in Fennoscandia and the Barents Sea during the last glacial cycle on glacial isostatic adjustment observations. Solid Earth 8, 955–968. https://doi.org/10.5194/se-8-955-2017.

van der Wal, W., Kurtenbach, E., Kusche, J., Vermeersen, B., 2011. Radial and tangential gravity rates from GRACE in areas of glacial isostatic adjustment. Geophys. J. Int. 187, 797–812. https://doi.org/10.1111/j.1365-246X.2011.05206.x.

Wang, H., 2000. Surface vertical displacements and level plane changes in the front reservoir area caused by filling the three gorges reservoir. J. Geophys. Res. Solid Earth 105, 13211–13220. https://doi.org/10.1029/2000JB900072.

Wdowinski, S., Bock, Y., Zhang, J., Fang, P., Genrich, J., 1997. Southern California permanent GPS geodetic array: spatial filtering of daily positions for estimating coseismic and postseismic displacements induced by the 1992 landers Earthquake. J. Geophys. Res. 102, 18057–18070. https://doi.org/10.1029/97JB01380.

Wessel, P., Smith, W.H.F., Scharroo, R., Luis, J., Wobbe, F., 2013. Generic mapping tools: improved version released. Eos, Trans. Am. Geophys. Union 94, 409–410. https://doi.org/10.1002/2013EO450001.

Williams, S.D.P., 2003. The effect of coloured noise on the uncertainties of rates estimated from geodetic time series. J. Geod. 76, 483–494. https://doi.org/10.1007/s00190-002-0283-4.

Williams, S.D.P., 2008. CATS: GPS coordinate time series analysis software. GPS Solut. 12, 147–153. https://doi.org/10.1007/s10291-10007-10086-10294.

Williams, S.D.P., Bock, Y., Fang, P., Jamason, P., Nikolaidis, R.M., Prawirodirdjo, L., Miller, M., Johnson, D.J., 2004. Error analysis of continuous GPS position time series. J. Geophys. Res. 109, 1–19. https://doi.org/10.1029/2003JB002741.

Wu, P., Steffen, H., Wang, H., 2010. Optimal locations for GPS measurements in North America and northern Europe for constraining glacial isostatic adjustment. Geophys. J. Int. 181, 653–664. https://doi.org/10.1111/j.1365-246X.2010.04545.x.

Zhang, J., Bock, Y., Johnson, H., Fang, P., Williams, S., Genrich, J., Wdowinski, S., Behr, J., 1997. Southern California permanent GPS geodetic array: error analysis of daily position estimates and site velocities. J. Geophys. Res. 102, 18035–18055. https://doi.org/10.1029/97JB01380.

Zhao, S., Lambeck, K., Lidberg, M., 2012. Lithosphere thickness and mantle viscosity inverted from GPS-derived deformation rates in Fennoscandia. Geophys. J. Int. 190, 278–292. https://doi.org/10.1111/j.1365-246X.2012.05454.x.